



Title	Importance of Ekman transport and gyre circulation change on seasonal variation of surface dissolved iron in the western subarctic North Pacific
Author(s)	Nakanowatari, Takuya; Nakamura, Tomohiro; Uchimoto, Keisuke; Nishioka, Jun; Mitsudera, Humio; Wakatsuchi, Masaaki
Citation	Journal of Geophysical Research: Oceans, 122(5), 4364-4391 <a href="https://doi.org/10.1002/2016JC012354">https://doi.org/10.1002/2016JC012354</a>
Issue Date	2017-05-03
Doc URL	<a href="http://hdl.handle.net/2115/72718">http://hdl.handle.net/2115/72718</a>
Rights	Copyright [2017] American Geophysical Union.
Type	article
File Information	Journal of geophysical research oceans122_4364_4391.pdf



[Instructions for use](#)



## RESEARCH ARTICLE

10.1002/2016JC012354

## Key Points:

- Seasonal variation of dissolved Fe in the western subarctic North Pacific is studied using an OGCM coupled with simple biogeochemical model
- Lateral advection and vertical mixing contribute comparably to the increase of dissolved Fe during winter
- Ekman transport and upwelling/downwelling as well as the geostrophic current system is related to lateral advection process

## Correspondence to:

T. Nakanowatari,  
nakanowatari.takuya@nipr.ac.jp

## Citation:

Nakanowatari, T., T. Nakamura, K. Uchimoto, J. Nishioka, H. Mitsudera, and M. Wakatsuchi (2017), Importance of Ekman transport and gyre circulation change on seasonal variation of surface dissolved iron in the western subarctic North Pacific, *J. Geophys. Res. Oceans*, 122, 4364–4391, doi:10.1002/2016JC012354.

Received 20 SEP 2016

Accepted 26 APR 2017

Accepted article online 3 MAY 2017

Published online 25 MAY 2017

## Importance of Ekman transport and gyre circulation change on seasonal variation of surface dissolved iron in the western subarctic North Pacific

Takuya Nakanowatari<sup>1,2</sup> , Tomohiro Nakamura<sup>2</sup>, Keisuke Uchimoto<sup>3</sup> , Jun Nishioka<sup>2</sup> , Humio Mitsudera<sup>2</sup>, and Masaaki Wakatsuchi<sup>2</sup>

<sup>1</sup>National Institute of Polar Research, Tachikawa, Japan, <sup>2</sup>Institute of Low Temperature Science, Hokkaido University, Sapporo, Japan, <sup>3</sup>Research Institute of Innovative Technology for the Earth, Kyoto, Japan

**Abstract** Iron (Fe) is an essential nutrient for marine phytoplankton and it constitutes an important element in the marine carbon cycle in the ocean. This study examined the mechanisms controlling seasonal variation of dissolved Fe (dFe) in the western subarctic North Pacific (WSNP), using an ocean general circulation model coupled with a simple biogeochemical model incorporating a dFe cycle fed by two major sources (atmospheric dust and continental shelf sediment). The model reproduced the seasonal cycle of observed concentrations of dFe and macronutrients at the surface in the Oyashio region with maxima in winter (February–March) and minima in summer (July–September), although the simulated seasonal amplitudes are a half of the observed values. Analysis of the mixed-layer dFe budget indicated that both local vertical entrainment and lateral advection are primary contributors to the wintertime increase in dFe concentration. In early winter, strengthened northwesterly winds excite southward Ekman transport and Ekman upwelling over the western subarctic gyre, transporting dFe-rich water southward. In mid to late winter, the southward western boundary current of the subarctic gyre and the outflow from the Sea of Okhotsk also bring dFe-rich water to the Oyashio region. The contribution of atmospheric dust to the dFe budget is several times smaller than these ocean transport processes in winter. These results suggest that the westerly wind-induced Ekman transport and gyre circulation systematically influence the seasonal cycle of WSNP surface dFe concentration.

### 1. Introduction

The western subarctic North Pacific (WSNP) is one of the most biologically productive regions in the world, especially during the bloom season that extends from spring into summer in the Oyashio region [Saito et al., 2002; Isada et al., 2010]. The high level of primary production in the WSNP leads to a very large biological drawdown of pCO<sub>2</sub> [Takahashi et al., 2002] and it supports considerable fishery production [Sakurai, 2007]. Thus, to understand the mechanisms that sustain the seasonal cycle of primary production is of considerable importance to both the forecasting of air-sea CO<sub>2</sub> flux and the management of fishery resources.

The subarctic North Pacific is one of the major high-nutrient low-chlorophyll (HNLC) regions in the world's oceans, and phytoplankton growth is sensitive to dissolved iron (dFe) concentration, which is a limiting micronutrient in the control of phytoplankton growth [Martin et al., 1989; Tsuda et al., 2003; Boyd et al., 2004]. One possible source of dFe in the ocean is atmospheric dust. In fact, the large seasonal variation in pCO<sub>2</sub> and nutrient drawdown in the WSNP, in comparison with the eastern subarctic North Pacific, is qualitatively consistent with the longitudinal difference of the surface flux of dust containing Fe, which originates primarily in the Gobi Desert in the Eurasian continent [Duce and Tindale, 1991; Mahowald et al., 2005; Measures et al., 2005].

Oceanic flux from the continental shelf also plays an essential role in the formation of high dFe concentrations in the subsurface to intermediate layer of the WSNP. A number of observations have shown high concentrations of dFe over the continental shelves, some of which are likely to be advected into the open ocean [Lam et al., 2006; Nishioka et al., 2007, 2013; Lam and Bishop, 2008; Cullen et al., 2009]. Numerical experiments support the hypothesis that lateral transport of sedimentary dFe from the continental margins into the open ocean causes high concentrations of dFe in the WSNP [Misumi et al., 2011]. In particular, the

© 2017. The Authors.

This is an open access article under the terms of the Creative Commons Attribution-NonCommercial-NoDerivs License, which permits use and distribution in any medium, provided the original work is properly cited, the use is non-commercial and no modifications or adaptations are made.

**Table 1.** Parameters of the Biogeochemical Model That Used Different Values to *Uchimoto et al. [2014]*

Definition	<i>Uchimoto et al. [2014]</i>	This Study
Sedimentary iron flux	1.0 (<300 m over the entire continental shelf) μmol Fe m <sup>-2</sup> d <sup>-1</sup>	0.5 (<300 m over the northwestern shelf) μmol Fe m <sup>-2</sup> d <sup>-1</sup>
Euphotic zone	135 m	50 m
Iron half saturation constant ( $K_{Fe}$ )	0.5 nM	0.12 nM

thermohaline and wind-driven ocean circulations that originate from the northwestern shelf in the Sea of Okhotsk are essential for the transport of dFe into the North Pacific [*Uchimoto et al., 2014*]. However, previous studies have focused on dFe concentration in intermediate water and, thus, dFe concentration at the surface has not been examined fully.

*Nishioka et al. [2011]* reported that time series data from the Oyashio region show clear seasonal variation in the dFe concentration in the mixed layer, and they suggested that the vertical entrainment process is crucial for the dFe budget in winter because it draws up subsurface dFe-rich water originating from the continental shelves. *Shigemitsu et al. [2012]* investigated the seasonal dFe cycle in the Oyashio region using a 1-D ecosystem model. They also found that more dFe is supplied to the mixed layer from the subsurface layer by wintertime entrainment than by the dissolution of atmospheric dust. However, these studies focused on the vertical 1-D mechanisms of ocean physics and, therefore, the role of lateral advection in the seasonal variability of surface dFe concentration in the WSNP, including the Oyashio region, was not evaluated.

Here we examine the mechanisms controlling the seasonal variability of surface dFe concentration in the WSNP, using an ocean general circulation model (OGCM) coupled with a biogeochemical model [*Uchimoto et al., 2014*]. The model and experimental settings are described in section 2. In section 3, the seasonal variation of the biogeochemical model is evaluated in comparison with observational data. In section 4, we perform a budget analysis of surface dFe concentration in the Oyashio and western subarctic regions on a seasonal timescale. We further explore the physical process controlling the seasonal variation of the mixed-layer dFe concentration. In section 5, we evaluate the contribution of dFe sources to surface dFe concentrations. Section 6 presents a summary and discussion.

## 2. Description of Model, Experimental Setting, and Observational Data

The biogeochemical-physical coupled model used in this study is based on a regional OGCM of the WSNP that includes the Sea of Okhotsk [*Uchimoto et al., 2011; Nakanowatari et al., 2015*], coupled with a biogeochemical model that includes phosphorous (PO<sub>4</sub>) and dFe cycles [*Parekh et al., 2005*]. Its physical part, which is a regional OGCM with sea ice in the WSNP and the Sea of Okhotsk, successfully simulated the wind-driven and thermohaline circulations on seasonal to decadal timescales [*Uchimoto et al., 2011; Nakanowatari et al., 2015*]. By coupling this OGCM with a biogeochemical model that incorporates a dFe cycle forced by two major sources (atmospheric dust and the northwestern shelf of the Sea of Okhotsk), *Uchimoto et al. [2014]* successfully simulated the spatial distribution of dFe concentration in the intermediate water both in and around the Sea of Okhotsk.

For this biogeochemical model, we modified some dFe parameters and the irradiance condition in the mixed layer from the original version to account for the vertical movement of phytoplankton as a result of the deepening of the mixed-layer depth (MLD) in winter. The modified parameter values for the biogeochemical model are listed in Table 1. The setting and configurations for the physical and biogeochemical models are revisited in the following section. For a detailed description of the physical and biogeochemical models, see *Uchimoto et al. [2011, 2014]* and *Nakanowatari et al. [2015]*.

### 2.1. Ocean Model

The physical model used in this study was the Center for Climate System Research Ocean Component Model coupled with a sea ice model (COCO ver. 3.4) [*Hasumi, 2006*]. The ocean model solves the primitive equation system under Boussinesq and hydrostatic approximations, and it uses a  $\sigma_0 z$  hybrid vertical coordinate with a free surface. The sea ice model was based on a two-category thickness representation, zero-layer thermodynamics [*Semtner, 1976*], and dynamics with elastic-viscous-plastic rheology [*Hunko and Dukowicz, 1997*]. There were 51 levels in the vertical direction with thicknesses increasing to the deeper layers (1–30 m intervals for the wintertime mixed layer in the subarctic gyre), the horizontal

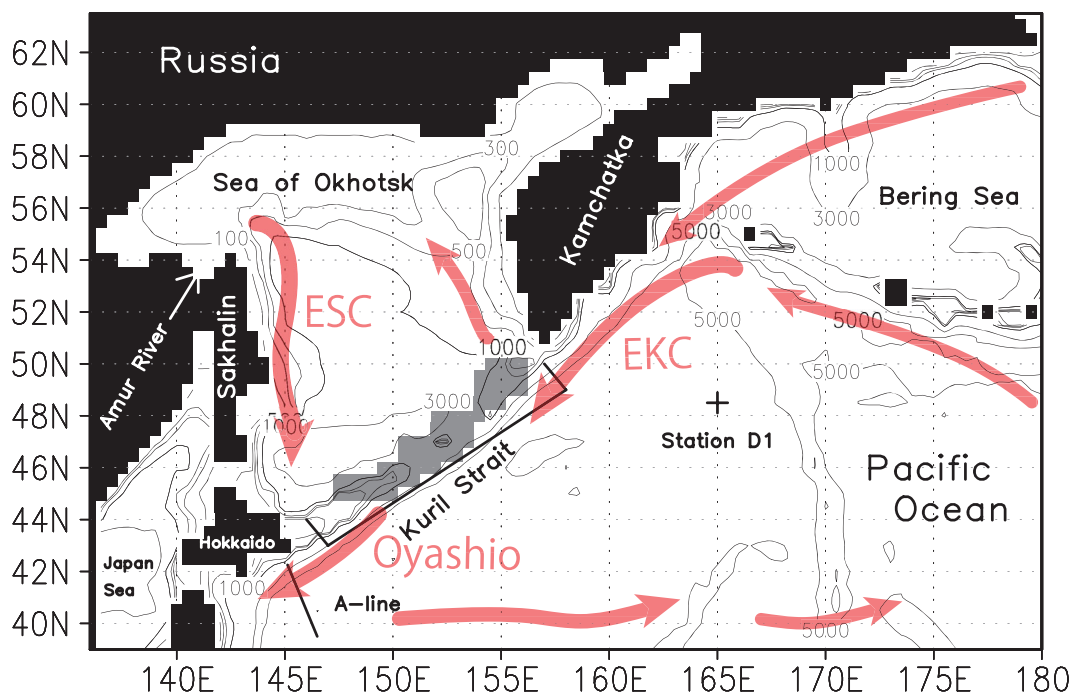


**Figure 1.** (a) Model topography. Contours indicate depths of 100, 300, 500, 1000, 3000, and 5000 m. Shading indicates region where the vertical diffusive coefficients are enhanced. The wind-driven gyre circulation and its western boundary currents are shown by arrows for the East Sakhalin Current (ESC), the Oyashio current (Oyashio), and the East Kamchatka Current (EKC). The locations for the A-line and station D1 are indicated by a dotted line and cross mark, respectively.

resolution was  $0.5^\circ \times 0.5^\circ$ , and the model domain covered the Okhotsk Sea and the western subarctic region (Figure 1a).

To represent the seasonal cycles of heat and salt fluxes from the subtropical gyre and subarctic gyre, we restored the temperature and salinity at the lateral boundary with a 1 day restoring time, using the monthly mean climatology of the World Ocean Atlas 2001 (WOA2001) [Boyer et al., 2002; Stephens et al., 2002]. Sea surface height was also restored at the lateral boundary to the climatological daily mean sea surface height obtained from the North Pacific model with the same configurations as our model. To avoid the drifting problem of sea surface salinity (SSS), we weakly restored SSS to the values of the WOA2001 with a 60 day restoring time. However, to represent the effect of ventilation induced through the brine rejection of sea ice formation, the restoring of SSS was not applied in the Okhotsk Sea north of 53°N from December to the following April. At levels deeper than about 2000 m, temperature and salinity were restored to the values of the WOA2001 with a 10 day restoring time, to represent the abyssal circulation.

To represent the effects of tidal mixing along the Kuril Strait, the vertical diffusivity coefficient ( $K_z$ ) was enhanced by  $20 \text{ cm}^2 \text{ s}^{-1}$  in the Kuril Strait from the surface to a depth of 500 m (Figure 1b) [Nakanowatari et al., 2015]. The values and extent of  $K_z$  were comparable with those from a nonhydrostatic model simulation [Nakamura and Awaji, 2004] and a barotropic tide model [Tanaka et al., 2010]. We also applied the  $K_z$  value in the Kuril Strait adopted by Uchimoto et al. [2011, 2014] but the results were essentially unchanged. Thus, we consider that our conclusion is not sensitive to the value of  $K_z$  in the Kuril Strait.

## 2.2. Biogeochemical Model

The biogeochemical model adopted in this study consisted of  $\text{PO}_4$  and dFe cycles [Parekh et al., 2005]. The concentrations of  $\text{PO}_4$  and dissolved organic phosphorus (DOP) were governed by the advection, diffusion, and sink/source terms related to biological uptake and remineralization processes, as follows:

$$\frac{\partial PO_4}{\partial t} = Adv(PO_4) + Diff(PO_4) + \lambda PO_4 + \begin{cases} -\Gamma & \\ -\frac{\partial F(z)}{\partial z} (below euphotic zone), & v\Gamma \\ 0 (below euphotic zone) & \end{cases}, \quad (1)$$

$$\frac{\partial DOP}{\partial t} = Adv(DOP) + Diff(DOP) - \lambda DOP + \begin{cases} v\Gamma & \\ 0 (below euphotic zone) & \end{cases},$$

where  $Adv$  represents the flux convergence owing to large-scale flow,  $Diff$  represents the flux convergence owing to mixing by subgrid-scale eddies,  $\lambda$  represents the timescale for remineralization ( $1/\lambda = 6$  month),  $\Gamma$  represents the biological uptake of  $PO_4$ ,  $F$  represents the vertical flux of remineralized particulate organic phosphorus below euphotic zone with the form of *Martin et al.*'s [1987] power law ( $F(z) = \int_{h_e}^0 (1-v)\Gamma dz (z/h_e)^{-b}$ ), and  $v$  is the fraction of phosphate (0.67) that enters the surface DOP pool. Equation (1) means that part of the biological uptake of  $PO_4$  in the euphotic layer ( $v\Gamma$ ) enters the DOP pool at the same grid point. The residual ( $(1-v)\Gamma$ ) is exported as particulates to the aphotic layer, and the remineralization was expressed as the convergence of its flux. DOP was remineralized continuously with an e-folding scale ( $\lambda$ ) in both the euphotic and the aphotic layers.

The biological uptake of  $PO_4$ ,  $\Gamma$ , was formulated using Michaelis-Menten kinetics with  $PO_4$ , dFe, and light limitations, as follows:

$$\Gamma = \alpha \frac{PO_4}{PO_4 + K_{PO_4}} \frac{dFe}{dFe + K_{dFe}} \frac{I}{I + K_l}, \quad (2)$$

where  $\alpha$  is the maximum export rate, and  $K_{PO_4}$ ,  $K_{dFe}$ , and  $K_l$  represent the half saturation constants for  $PO_4$ , dFe, and light, respectively.  $K_l$  was set to  $30 \text{ W m}^{-2}$ , which is identical to the original version of *Parekh et al.* [2005]. Based on the sensitivity experiments on  $K_{dFe}$  and  $\alpha$  performed by *Uchimoto et al.* [2014], we set  $K_{PO_4}$ ,  $K_{dFe}$ , and  $\alpha$  to  $0.5 \mu\text{M}$ ,  $0.12 \text{ nM}$ , and  $1.0$ , respectively. In this model, it is assumed that phytoplankton takes up and releases P and dFe in a constant ratio (please see the details below).

Daily mean data of shortwave radiation flux were applied as irradiance ( $I_0$ ). In this study, irradiance was modified to decay exponentially from the sea surface downward with an e-folding scale ( $h_e$ ), as follows:

$$I = I_0 e^{-\frac{z}{h_e}}. \quad (3)$$

As our focus was on the surface material cycle in high-production areas, we modified  $h_e$  from the original value to  $10.86 \text{ m}$ , which made the irradiance at  $50 \text{ m}$  (i.e., the bottom of the euphotic layer) about 1% that at the sea surface. This value ( $50 \text{ m}$ ) is within the range for the euphotic layer adopted in earlier modeling studies, e.g.,  $38 \text{ m}$  [*Siegel et al.*, 2002] to  $79 \text{ m}$  [*Sarmiento et al.*, 1993]. In sea ice regions, the decay of irradiance is estimated as a function of albedo, ice thickness, and decay scale in ice [*Perovich*, 1998]. Furthermore, to express indirectly the migration of phytoplankton, we artificially average the irradiance strength in the mixed layer, as follows:

$$I' = \frac{1}{h_{MLD}} \int_{h_{MLD}}^0 I dz, \quad (4)$$

where  $h_{MLD}$  is the MLD, which is determined by the density change from the ocean surface of  $0.125\sigma_\theta$ . dFe concentration was governed by the advection and diffusion terms, with source/sink terms related to biological uptake and external source/sink terms, as follows:

$$\frac{\partial dFe}{\partial t} = Adv(dFe) + Diff(dFe) + \lambda DOP \times R_{dFe} + \underbrace{S_{dFe} + J_{dFe} + Sed_{dFe}}_{External Source/Sink} + \begin{cases} -\Gamma R_{dFe} & \\ -\frac{\partial F(z)}{\partial z} R_{dFe} (below euphotic zone) & \end{cases}, \quad (5)$$

where  $R_{dFe}$  is the proportional coefficient of the dFe:P ratio, which is fixed to  $0.47 \text{ mmol:1 mol}$ ,  $S_{dFe}$  and  $Sed_{dFe}$  are, respectively, the external sources of atmospheric dust and shelf bottom sediments in the Sea of Okhotsk, and  $J_{dFe}$  is the sink by scavenging. The biological uptake, export, and remineralization terms are proportional to those in the  $PO_4$  equations with the proportional coefficient of  $R_{dFe}$ . The dFe is assumed to be the sum of the free dFe' and complexed dFeL forms, where L represents dFe binding organic ligands.

The eolian dust flux data were derived from the monthly mean dust deposition provided by *Mahowald et al.* [2005]. This data set is a composite of dust flux data from three different atmospheric models with more than 10 years of simulations. We applied the dFe flux based on the assumption that Fe is 3.5 wt % of dust and that it dissolves instantaneously at the sea surface (the upper most grid) with a solubility in seawater of 1%, according to the sensitivity experiments of *Uchimoto et al.* [2014]. The distribution of annual mean dFe flux is presented in Figure 2a. It is noted that the dust flux was transmitted to the sea surface in sea ice in this study. As we are concerned with examining the dFe budget in the WSNP, the accumulation of dust in sea ice is not considered to be significant.

The sedimentary flux of dFe was applied on the bottom (the deepest grid) in the northwestern shelf region shallower than 300 m (Figure 2b) to represent the dFe input from the Amur River (shown in Figure 1). In fact, a previous model simulation indicated that sedimentary flux in the northwestern shelf plays an essential role in forming the high dFe concentration in the intermediate layer [*Uchimoto et al.*, 2014]. Based on our sensitivity experiments on the magnitude of sedimentary flux, we used a constant value of  $0.5 \mu\text{mol Fe m}^{-2} \text{d}^{-1}$ , which is comparable with the flux values adopted by earlier studies [*Moore et al.*, 2004; *Parekh et al.*, 2008; *Uchimoto et al.*, 2014]. It is noted that the dissolution process of resuspended particles is not explicitly considered for simplicity. Therefore, the dFe flux applied in this model includes both the dFe directly supplied from the Amur River and sediment and the dFe from the resuspended particles in the sediment. The sedimentary flux of dFe from the eastern shelf of the Bering Sea was given through a lateral boundary condition that is described later.

The scavenging rate is calculated by the formulation of  $J_{Fe} = -\tau k_0 C_p^\phi dFe'$  where  $C_p$  is the particulate concentration calculated by  $F(z) = C_p W_{sink}$ ,  $k_0$  is the scavenging rate with no limitation by particles,  $\phi$  is an empirically determined constant coefficient,  $\tau$  is the scaling factor, and  $W_{sink}$  is the particulate sinking rate. These parameter values are identical to those proposed by *Parekh et al.* [2005].  $dFe'$  was controlled by an equilibrium relationship  $K_{dFeL} L = [dFeL]/[dFe'] [L']$ , where  $K_{dFeL}$  is the ligand conditional stability constant. Thus, the only  $dFe'$  was susceptible to scavenging rate. According to recent model simulations focused on the North Pacific [*Misumi et al.*, 2011; *Uchimoto et al.*, 2014], we set the total ligand (sum of  $FeL$  and  $L'$ ) to be 1.2 nM.

Usually, ecosystem model in the subarctic North Pacific uses nitrate as limiting macronutrient [e.g., *Kawamiya et al.*, 2000]. Our model assumes nitrate and phosphate to be in a constant Redfield ratio, as nitrate is not explicitly modeled. This assumption appears valid, because primary production in our model domain is limited by the same macronutrient everywhere. Furthermore, our model constituted a simple nutrient-type biogeochemical model in which the amount of phytoplankton was not explicitly predicted; thus, phytoplankton growth and mortality were assumed balanced. Therefore, the rate of uptake of  $PO_4$  in the blooming season and its duration appear underestimated and long in the coastal region, respectively. Nonetheless, this simple model enabled us to examine the mechanism responsible for the timing of the wintertime increase in dFe concentration in the WSNP including the Oyashio region, because the biological uptake was likely to be small due to light limitation in winter.

As lateral boundary condition,  $PO_4$  concentration was restored to the monthly means of the World Ocean Atlas 2009 (WOA09) [*Garcia et al.*, 2010] in a similar manner to temperature and salinity. DOP was set to be zero along the lateral boundaries to avoid the artificial accumulation of DOP near the boundaries by reflection of DOP-rich water. The lateral boundary values of dFe concentration were identical to those of *Uchimoto et al.* [2014], who produced them by merging observational data from the Bering Sea by *Takata et al.* [2005, 2008] and from the North Pacific by *Nishioka et al.* [2007, 2013], and based on the results of a simulation by *Misumi et al.* [2011]. The vertical profiles for dFe concentrations at the southern boundary in the North Pacific show minimum ( $\sim 0.1 \text{ nM}$ ) at 10 m depth, which increases with depth and reaches the maximum value ( $\sim 1.0 \text{ nM}$ ) at around 900 m depth. In the Japan Sea, the vertical profile of dFe concentration is similar to the North Pacific, but the dFe concentration at the intermediate depth is somewhat lower ( $\sim 0.7 \text{ nM}$ ). In the eastern boundary (the Bering Sea), the dFe concentration are minimum ( $\sim 0.2 \text{ nM}$ ) at the surface, which increases with depth and reaches the maximum ( $\sim 1.5 \text{ nM}$ ) at the bottom. These lateral boundary conditions of dFe concentration were temporally constant and, thus, there was no seasonal variation.

### 2.3. Experimental Setting

The physical part of the model was first integrated for 50 years from the initial condition based on the climatological temperature and salinity of WOA2001, under surface forcing of the climatological daily mean

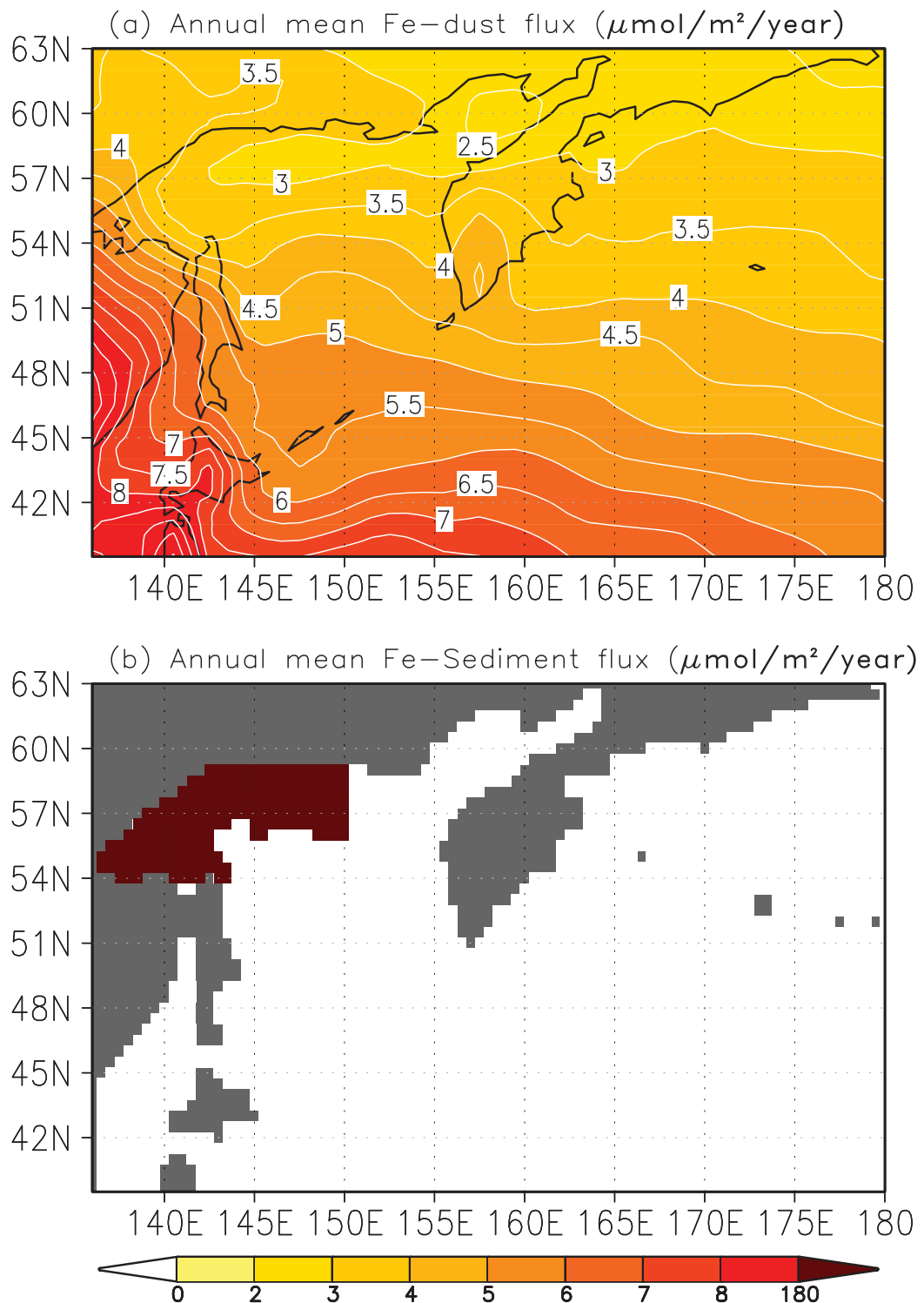


**Figure 2.** Spatial distribution of annual mean dFe flux ( $\mu\text{mol m}^{-2} \text{yr}^{-1}$ ) from (a) atmospheric dust and (b) sediment in the northwestern shelf region applied to the model.

atmospheric data of the Ocean Model Intercomparison Project (OMIP) [Röske, 2001]. The OMIP data are constructed from ECMWF reanalysis data from 1957 to 2001 with latitudinal and longitudinal resolution of  $1.125^\circ$ . From the physical condition in the final year of the spin-up, the coupled physical-biogeochemical

model was integrated from the initial condition based on the climatological  $\text{PO}_4$  of WOA2009, no initial DOP, and dFe values for 27 years under the OMIP surface forcing. This integral time might appear short for the spin-up of the intermediate circulation; however, it was considered sufficient for the surface circulation, which was the focus of this study, to reach a steady state. This experiment is hereafter defined as the control case. In this study, we used the monthly mean fields in the final year of the spin-up integration when the spatial distribution of  $\text{PO}_4$  had almost reached equilibrium.

#### 2.4. Observational Data

To evaluate the climatological features of  $\text{PO}_4$  in the model results, we used the summertime (July–September) statistical mean of  $\text{PO}_4$  derived from the WOA2009. As climatological 3-D data of dFe concentration in the entire domain of the WSNP were not available, we alternatively used dFe concentration data observed at the station D1 ( $48.5^\circ\text{N}$ ,  $165^\circ\text{E}$ , shown in Figure 1) in October 2003 [Nishioka *et al.*, 2007]. For the Oyashio region, we used dFe concentration data at seven stations (A4, A5, A7, A9, A11, A13, and A15) along the A-line ( $39.5^\circ\text{N}$ ,  $146.5^\circ\text{E}$  to  $42.25^\circ\text{N}$ ,  $145.125^\circ\text{E}$ , shown in Figure 1) observed in January 2005 [Nishioka *et al.*, 2011], where the A-line is the repeated hydrographic cross section operated by the Japan Fisheries Research and Education Agency [Saito *et al.*, 2002]. To evaluate the seasonal variation of dFe concentration in the Oyashio region, we also used the time series of monthly mean dFe concentrations, which were derived from one to eight cruises undertaken annually over a 6 year period along the A-line [Nishioka *et al.*, 2011]. The dFe concentrations in the mixed layer were calculated by averaging the monthly data in the mixed layer, the bottom of which was determined by a density change from the ocean surface of  $0.125\sigma_0$ . We also used monthly means of net primary production data from 2002 to 2016 with a spatial resolution of 9 km, which were based on MODIS satellite data including surface chlorophyll concentrations and the vertically generalized production model [Behrenfeld and Falkowski, 1997].

### 3. Simulated $\text{PO}_4$ and Fe Concentrations at the Surface

#### 3.1. Annual Mean Field

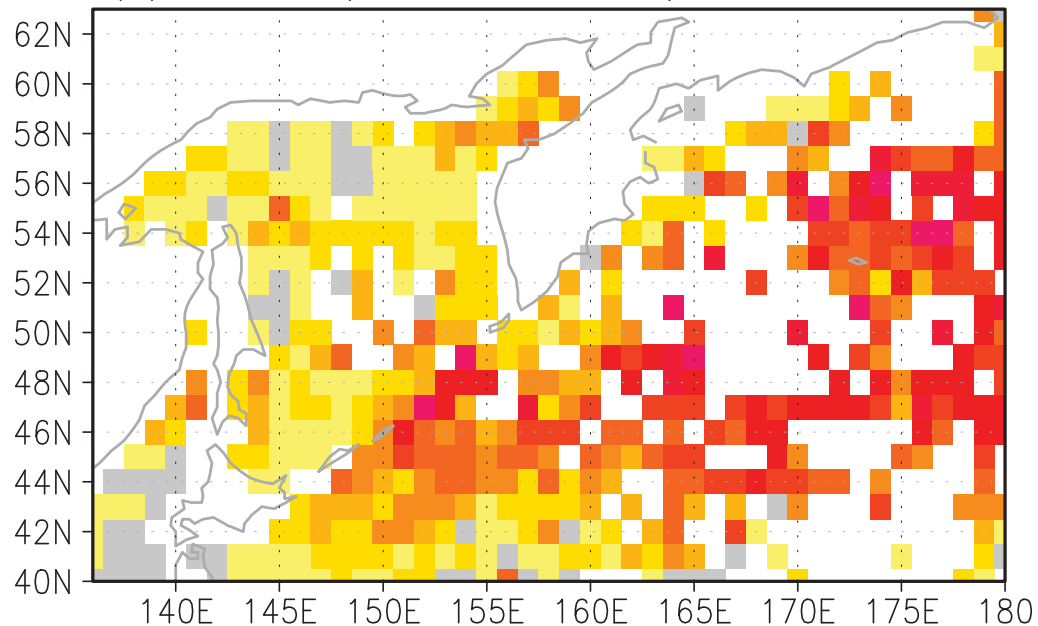
Before we examine the seasonal variation of  $\text{PO}_4$  and dFe in the WSNP including the Oyashio region, we evaluate the simulated climatological fields of  $\text{PO}_4$  and dFe by comparing them with observational data. Here we also show the sensitivity of these climatological fields to the euphotic layer depth, irradiance strength in the mixed layer, and value of  $K_{\text{Fe}}$  by comparing the control case with the earlier case [Uchimoto *et al.*, 2014]. The parameters in the control case that were different from the earlier case are summarized in Table 1.

Figures 3a and 3b compare the spatial patterns of surface  $\text{PO}_4$  concentration in the observed and simulated data in summer (July–September), a period during which observational data coverage is relatively dense. Relatively high values of  $\text{PO}_4$  concentration, higher than its half saturation constant ( $0.5 \mu\text{M}$ ), are features common in the WSNP (including the Bering Sea) in both data sets, although the modeled  $\text{PO}_4$  concentration is somewhat underestimated around  $48^\circ\text{N}$ ,  $165^\circ\text{E}$ . In the Sea of Okhotsk, the relatively low concentration of observed  $\text{PO}_4$  ( $<0.4 \mu\text{M}$ ) is also reproduced in the model. It is noted that a remarkably high concentration of  $\text{PO}_4$  ( $>1.5 \mu\text{M}$ ) is found along the Kuril Islands in both the observed and the simulated data sets. As tidal mixing is prominent in the Kuril Strait, the observed high concentration of  $\text{PO}_4$  in summer is likely maintained by strong mixing. Hydrographic observational data obtained recently from the Kuril Strait [Nishioka *et al.*, 2007] also support the high concentration of  $\text{PO}_4$  in summer.

Figure 4a shows the spatial distribution of simulated dFe concentration at the surface in summer (July–September). The dFe concentration is relatively high in the Sea of Okhotsk, with a maximum value of  $\sim 2 \text{ nM}$  around the mouth of the Amur River. The high value of dFe concentration extends southward with the East Sakhalin Current and reaches the Bussol Strait. The higher simulated dFe concentrations along Sakhalin Island are consistent with the observed spatial pattern of dFe concentration in summer [Nishioka *et al.*, 2014]. In the western subarctic region, the dFe concentration at the surface is  $<0.2 \text{ nM}$ , which is roughly consistent with the observed dFe concentration in summer [Nishioka *et al.*, 2007]. Thus, the summertime deficiency of dFe concentration in the western subarctic region was simulated in the model.

In the intermediate layer ( $26.8\sigma_0$  isopycnal surface), the dFe concentration is high on the northwestern shelf of the Sea of Okhotsk and along the East Sakhalin Current, similar to the surface dFe, with values  $>1 \text{ nM}$ .

PO<sub>4</sub> at surface (Jul.–Sep.)  
(a) WOA09 (statistical mean)



(b) Model (Control)

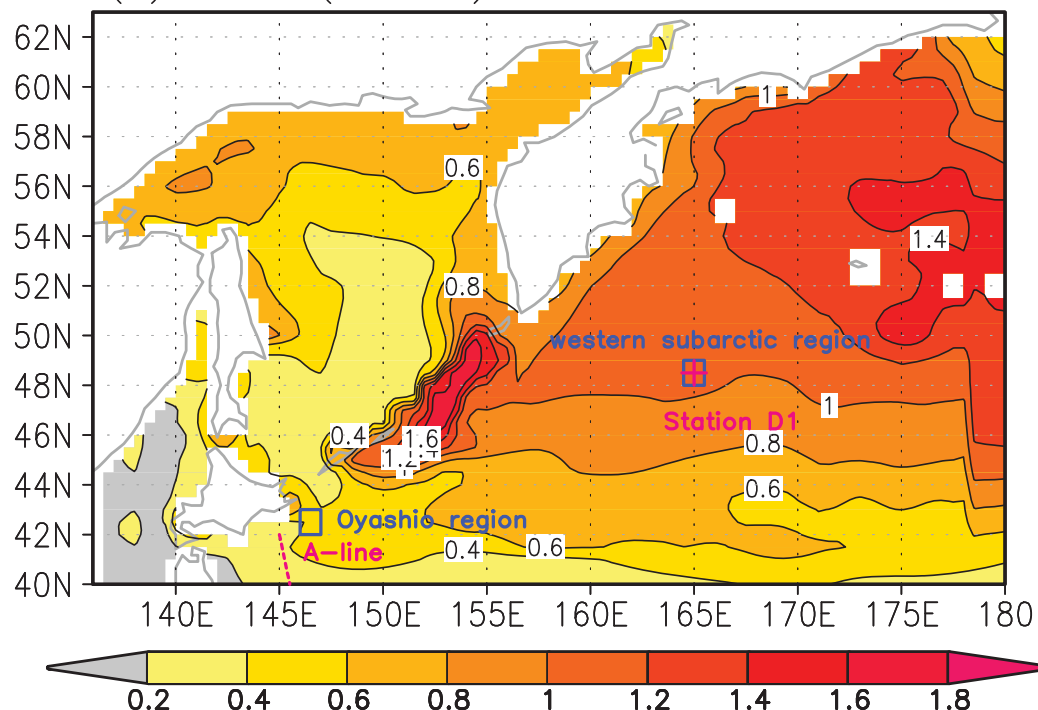


**Figure 3.** Spatial distribution of (a) observed and (b) simulated PO<sub>4</sub> ( $\mu\text{M}$ ) at the surface in July–September. The Oyashio [42°N–43°N, 146°E–147°E] and western subarctic regions [48°N–49°N, 164.5°E–165.5°E] are shown by the square blue boxes. The locations for the A-line and station D1 are indicated by a dotted line and cross mark, respectively.

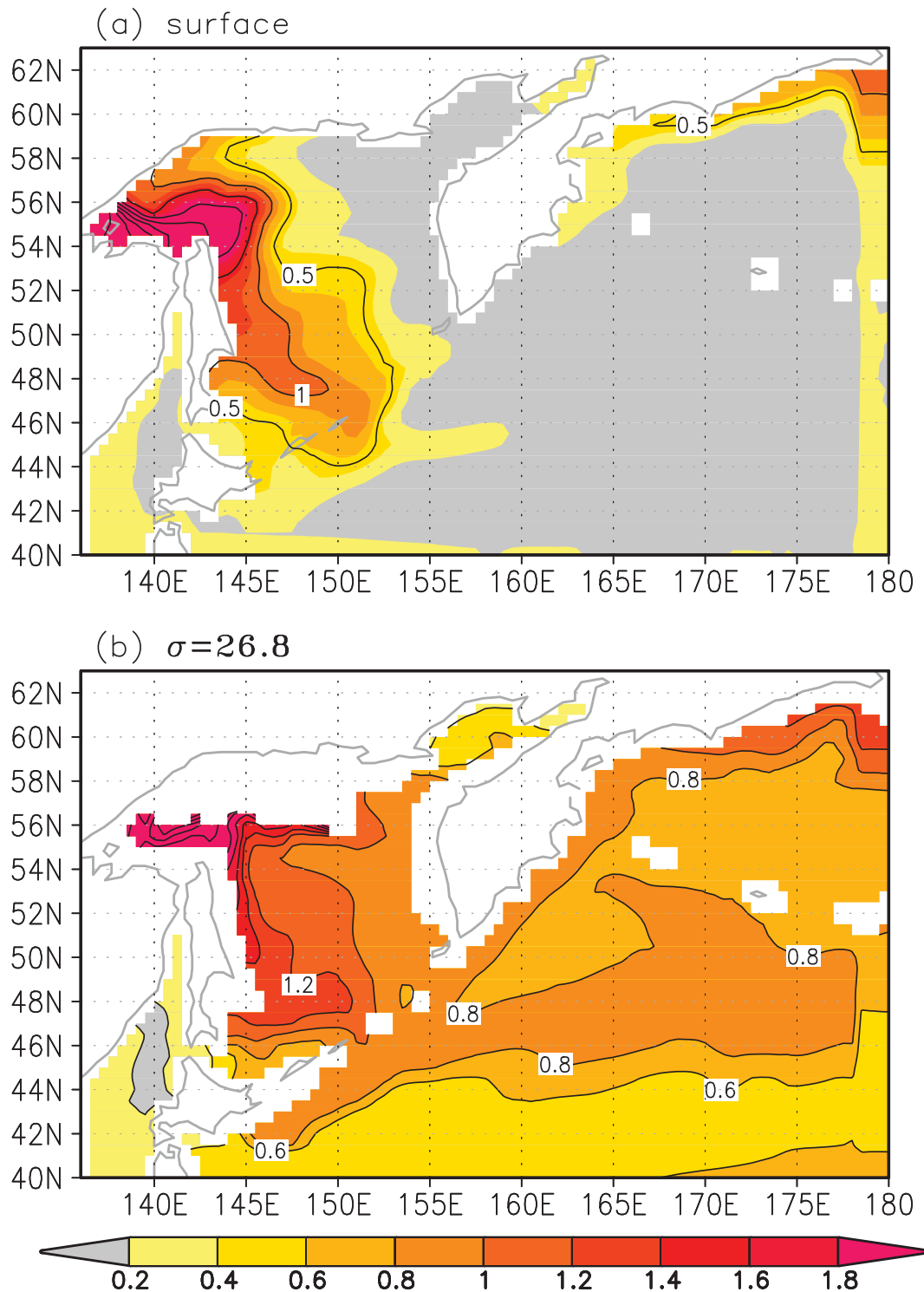


**Figure 4.** Spatial distribution of simulated dFe concentrations (nM) in July–September at (a) surface and (b)  $26.8\sigma_\theta$  isopycnal surface.

(Figure 4b). The relatively high dFe concentration (0.8 nM) extends into the western subarctic region, which is consistent with an earlier study [Uchimoto *et al.*, 2014]. dFe concentration  $>0.8$  nM is also found along the east coast of the Kamchatka Peninsula, extending from the northern part of the Bering Sea. As the high dFe concentration along the Kamchatka Peninsula is likely to intrude into the western subarctic region, this

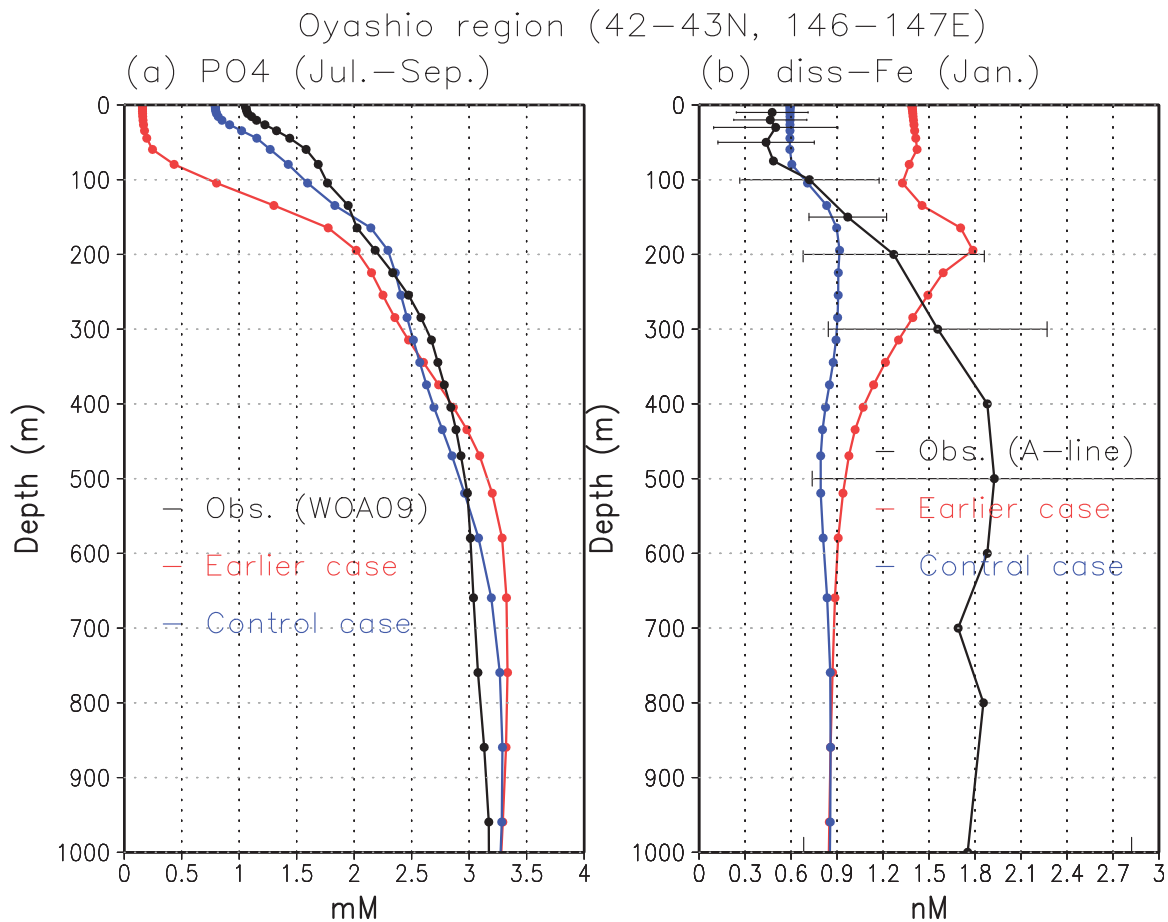


**Figure 5.** Vertical profiles of (a) PO<sub>4</sub> and (b) dFe concentrations in the Oyashio region (42°N–43°N, 146°E–147°E) from observed data (black) and model simulations (earlier and control cases). The observed profile of dFe is derived from the mean value of seven stations (A4, A5, A7, A9, A11, A13, and A15) in the A-line observed in January 2005 and the standard deviations are shown for the mean values at depths where the number of data is larger than 4. The geographical positions of the Oyashio region and A-line are shown by the rectangle (blue) and dotted line (magenta) in Figure 3b, respectively.

result suggests that dFe supplied from the Bering Sea partly contributes to the high dFe concentration in the intermediate water of the North Pacific.

Figure 5 shows the vertical profiles of simulated PO<sub>4</sub> and dFe concentrations in the Oyashio region (shown in Figure 3b). With the earlier version of the biogeochemical model parameters [Uchimoto et al., 2014], the simulated PO<sub>4</sub> concentration in the surface layer is relatively lower than the observed value, while the simulated dFe concentration is overestimated. In the control case, both the underestimation of PO<sub>4</sub> and the overestimation of dFe in the surface layer are improved. In particular, the simulated dFe in the upper layer (<300 m) is within the one standard deviations of observed values. On the other hand, the low bias of dFe concentration in the intermediate layer (deeper than 200 m) is not improved. As the focus of this study was on the seasonal variations in the mixed layer, which is shallower than 200 m in this region, the underestimation of dFe concentration in the deep layer was considered not to affect our results. For the western subarctic region (shown in Figure 3b), the observed data show that both PO<sub>4</sub> and dFe concentrations are low at the surface with a sharp gradient at around the depth of 200 m (Figure 6). These PO<sub>4</sub> and dFe gradients are basically identical to the earlier version of the model. It is noteworthy that the dFe in the model is depleted in late summer, whereas the simulated PO<sub>4</sub> concentration remains high, indicating that the western subarctic region has the characteristics of an HNLC region.

Next, we examine the rate of biological uptake of PO<sub>4</sub> ( $\Gamma$  in equation (2)) and compare it with the limiting factors of  $\Gamma$ . Here the limiting factors of  $\Gamma$  are PO<sub>4</sub>, dFe, and I, which are defined as  $PO_4/(PO_4 + K_{PO_4})$ ,  $dFe/(dFe + K_{dFe})$ , and  $I/(I + K_I)$ ; thus, these are proportional to PO<sub>4</sub>, dFe, and I, respectively. Since the limiting factor has a value between 0 and 1, the smaller values mean the strong limitation and vice versa, because the

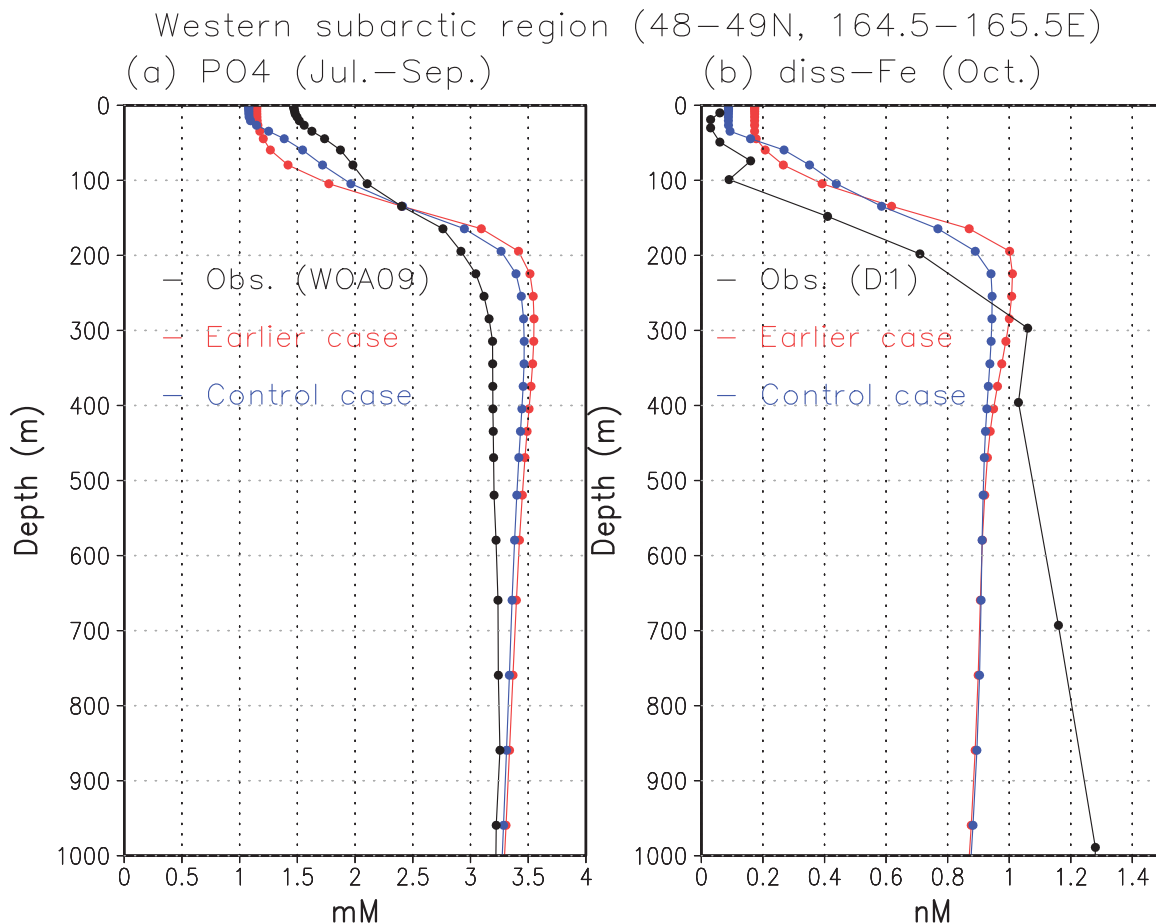
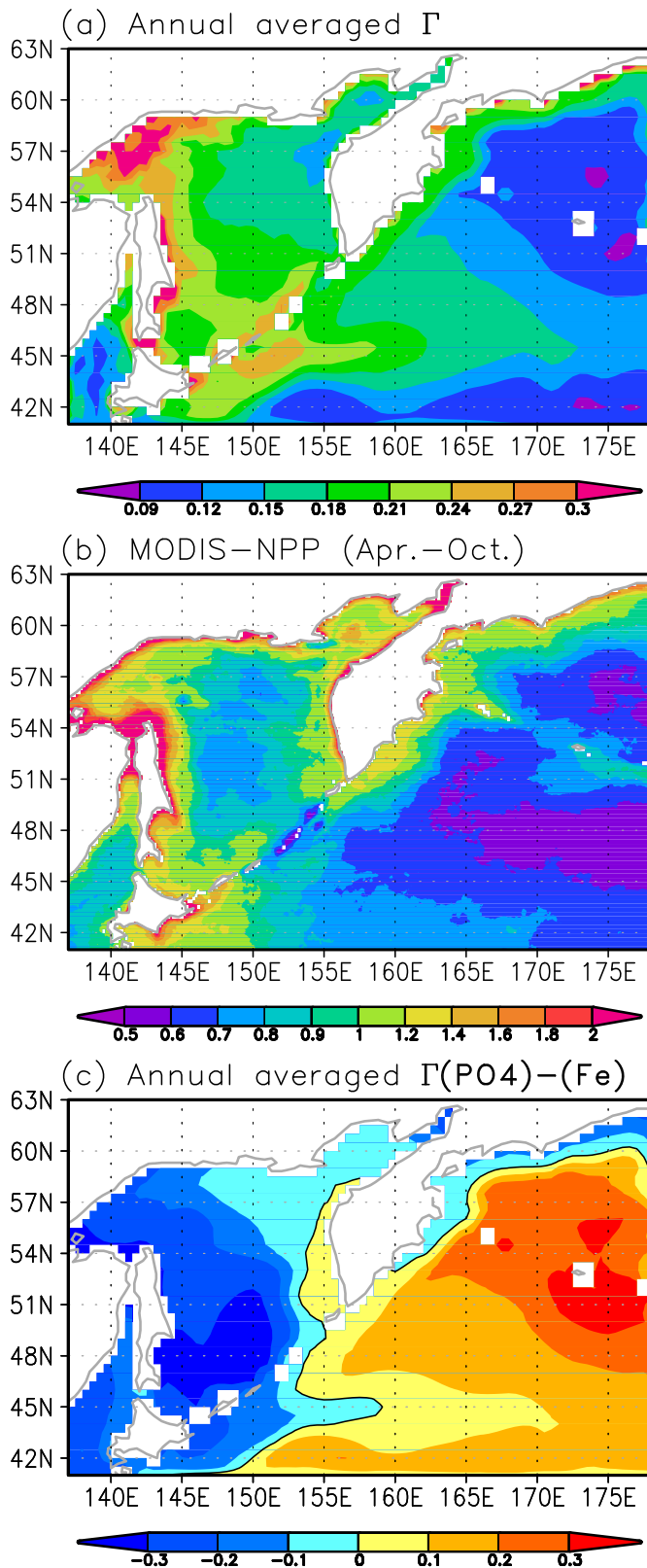


**Figure 6.** Vertical profiles of (a) PO<sub>4</sub> and (b) dFe concentrations in the western subarctic region (48°N–49°N, 164.5°E–165.5°E) from observed data (black) and model simulations (earlier and control cases). The observed profile of dFe concentration is based on the hydrographic observation at the station D1 (48.5°N, 165°E) observed in October 2003. The geographical position of the western subarctic region and station D1 are shown by the rectangle in Figure 3b.

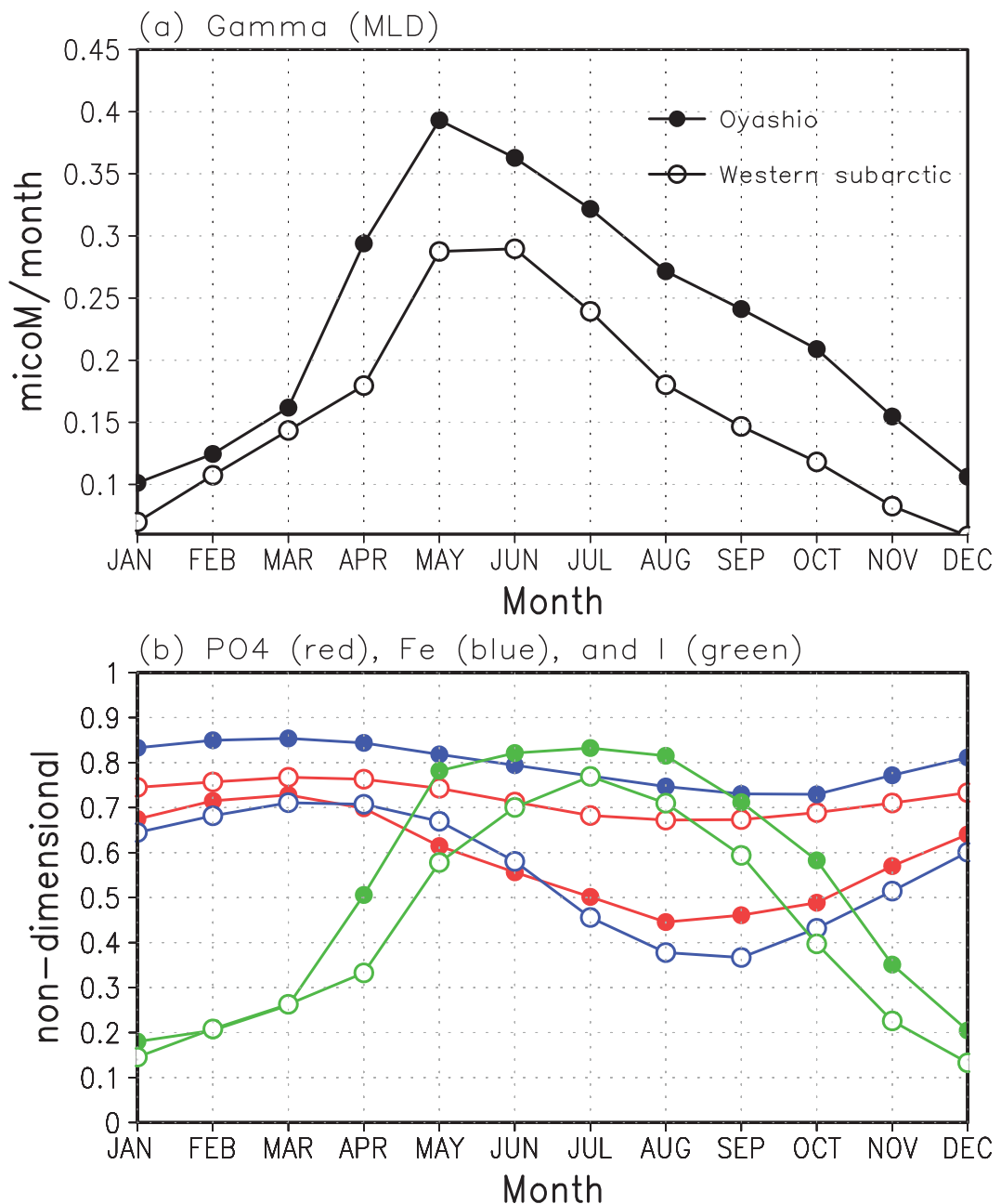
rate of biological uptake is determined by the multiplication of these values. In this biogeochemical model, the rates of phytoplankton growth and mortality are balanced and, thus, the rate of uptake of PO<sub>4</sub> ( $\Gamma$  in  $\mu\text{M/month}$ ) is approximately proportional to the net primary production.

Figure 7a shows the spatial pattern of the annual average of vertically integrated  $\Gamma$  in the mixed layer. Annually averaged  $\Gamma$  is relatively large along the coastline in the WSNP including the Oyashio region, where  $\Gamma$  reaches a maximum in May–June (not shown). This spatial pattern of  $\Gamma$  is basically consistent with the climatology of net primary production based on MODIS satellite data, although the cluster of high  $\Gamma$  in the Oyashio region in the model is somewhat shifted northward relative to the observed data (Figure 7b). In the basin area of the WSNP, excluding the coastal area, the limiting factors of  $\Gamma$  related to PO<sub>4</sub> concentration is higher than that for dFe concentration (Figure 7c), indicating that the rate of biological uptake is controlled by dFe concentration rather than by PO<sub>4</sub> concentration.

Figure 8a shows the seasonal cycle for the rate of uptake of PO<sub>4</sub> ( $\Gamma$ ) in the Oyashio and western subarctic regions. The monthly mean  $\Gamma$  shows a clear seasonal cycle with maxima in May–June in these regions. This seasonal cycle of  $\Gamma$  is consistent with those of chlorophyll concentration derived from hydrographic observation in the Oyashio region [Saito *et al.*, 2002]. In both regions, the seasonal cycle of  $\Gamma$  is controlled mostly by the strength of light. It is noted that the maximum value of  $\Gamma$  is relatively large in the Oyashio region compared with the western subarctic region. In this period (April–May), both dFe concentration and light intensity in the Oyashio region are higher than in the western subarctic region, but the phosphate concentration in the Oyashio region is lower (Figure 8b). Therefore, the higher amplitude of the seasonal variation in  $\Gamma$  is related to the higher dFe concentration, as well as to light intensity.



**Figure 7.** Spatial distribution of (a) annual averaged uptake rate of  $\text{PO}_4$  ( $\Gamma$ ) ( $\mu\text{mol/month}$ ) in the model and (b) climatology of net primary production (g C/m<sup>2</sup>/d) averaged from April to October based on MODIS satellite data during 2002–2016. (c) The difference between  $\text{PO}_4/(\text{PO}_4 + K_{\text{PO}_4})$  and  $\text{Fe}/(\text{Fe} + K_{\text{Fe}})$ , which are nondimensional indexes of the limiting factors for the biological uptake in the model, averaged in the mixed layer. When the positive (negative) value of this index indicates that the biological uptake is controlled by dFe ( $\text{PO}_4$ ) concentration. The contour indicates zero value.



**Figure 8.** Seasonal cycles of (a)  $\Gamma$  ( $\mu\text{mol}/\text{month}$ ) and (b) the limiting factors of  $\text{PO}_4$  ( $\text{PO}_4/(\text{PO}_4 + K_{\text{PO}_4}$ ) in red), dFe ( $\text{Fe}/(\text{Fe} + K_{\text{Fe}}$ ) in blue), and light ( $\text{I}/(\text{I} + K_{\text{I}}$ ) in green) averaged over the mixed layer in the Oyashio region (closed circles) and western subarctic region (open circles). The limiting factor has a value between 0 and 1, where the small value means strong limitation and vice versa. The areas of the Oyashio and western subarctic region are shown in Figure 7d.

### 3.2. Seasonal Variation

Figures 9a and 9b compare the seasonal cycles of  $\text{PO}_4$  and dFe with the seasonal cycle of the MLD in the Oyashio region (shown in Figure 3b). The simulated  $\text{PO}_4$  and dFe concentrations at the surface reveal a remarkable seasonal variation with maxima in winter (March) and minima in summer (September). The simulated MLD also shows a seasonal cycle with a maximum value of  $\sim 160$  m depth in March (Figure 9c). The simulated maximum MLD and its timing are comparable to the observed data along the A-line [Nishioka *et al.*, 2011]. The seasonal variations in dFe and MLD in the western subarctic region (Region B, shown in Figure 3b) also show seasonal cycles in dFe concentration and MLD, similar to those in the Oyashio region,

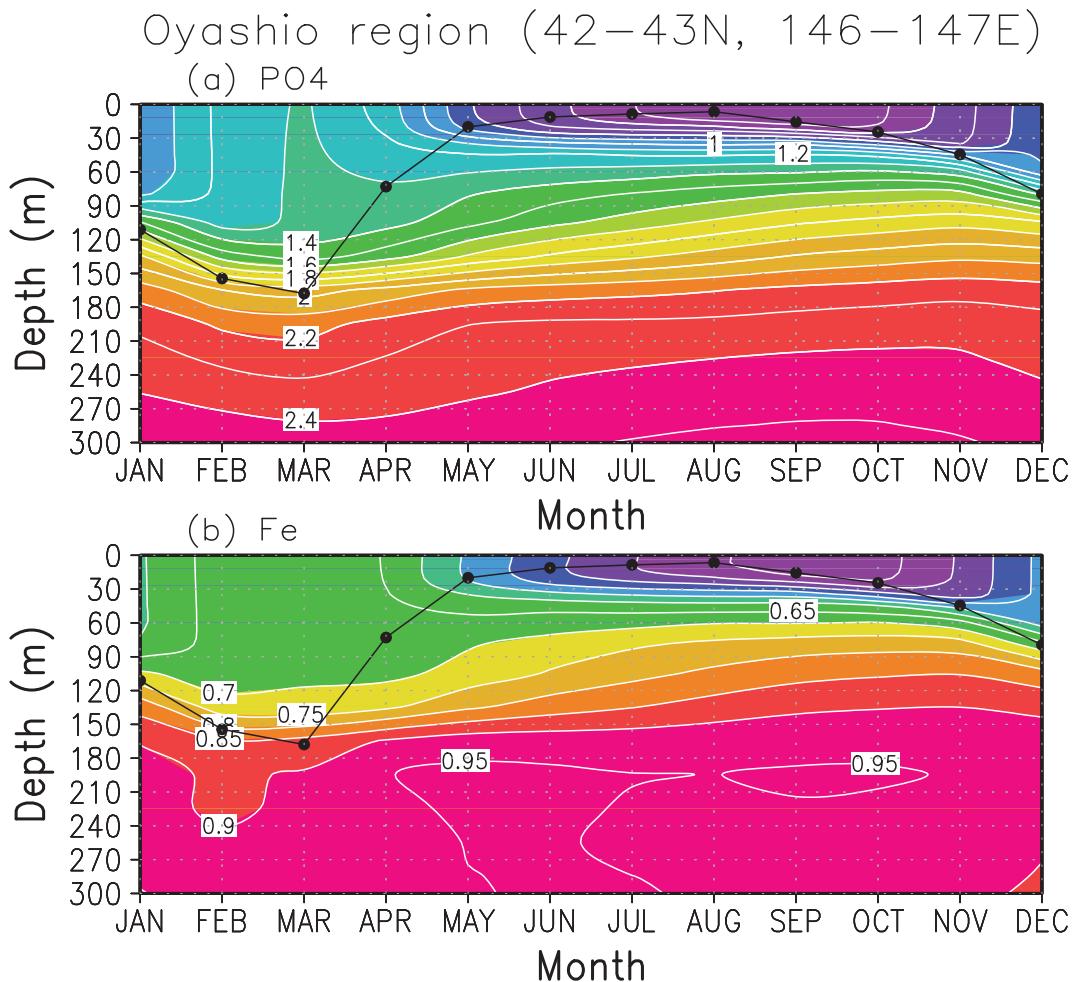


**Figure 9.** Seasonal cycles of simulated (a) PO<sub>4</sub> concentration ( $\mu\text{M}$ ) and (b) dFe concentration (nM) from the surface to 300 m depth in the Oyashio region. The monthly mean MLD is shown as closed circles in each figure.

although the occurrences of the maximum values are lagged by 1 month to those in the Oyashio region. The above comparisons between the simulated and observed data verify that the seasonal variations of dFe and the MLD are well represented in the model simulation.

The comparison between the simulated and observed averaged dFe concentrations in the mixed layer (Figure 10) indicates that the phase of seasonal variation in dFe in the Oyashio region is reproduced, although the seasonal amplitude, which is the difference between the maximum and minimum values ( $\sim 0.4 \text{ nM}$ ), is half that of the observed data. In particular, the decrease in dFe concentration in spring (April–May) is gradual. This could be related to the assumption that the maximum rate of uptake is fixed to a constant value ( $\alpha = 1.0 \mu\text{M}/\text{month}$ ); thus, the drastic decrease of dFe concentration related to spring bloom events is not quantitatively simulated in this biogeochemical model. Thus, although the dFe depletion in summer is underestimated in our experiment, it remains meaningful to examine the mechanisms controlling the increase in dissolved dFe during autumn and winter.

#### 4. Budget Analysis for Seasonal dFe Variation in the Mixed Layer

First, to clarify the physical processes responsible for the seasonal variation of dFe in the mixed layer, we evaluate the individual terms in the dFe tendency equation averaged over the monthly mean MLD,

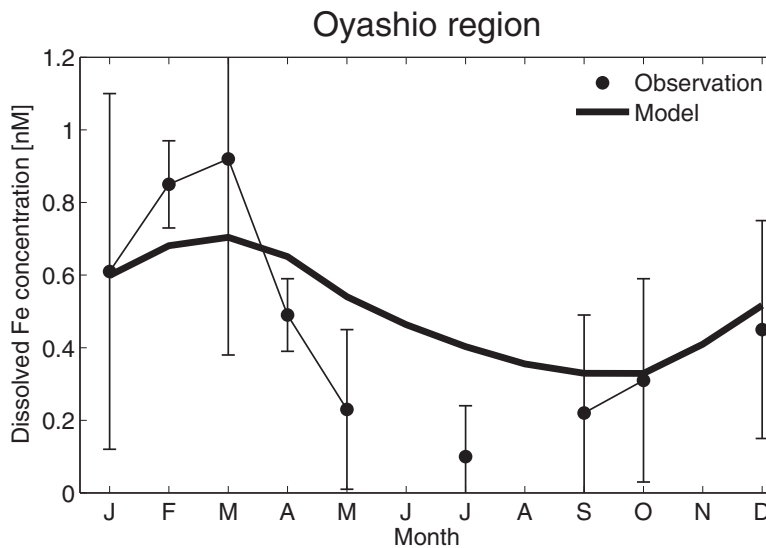


**Figure 10.** Observed (circles) and simulated dFe concentration averaged over the mixed layer from the simulation (solid line) in the Oyashio region. The observed data were calculated from the monthly mean dFe concentrations along the A-line [Nishioka et al., 2011]. The standard deviations of the monthly mean values are shown by error bars.

$$\frac{1}{MLD} \int_{MLD} \frac{\partial Fe}{\partial t} dz = \frac{1}{MLD} \int_{MLD} (ADV + MIX + BIO + SED + SFX) dz,$$

$$ADV = -\nabla \cdot (\bar{v} Fe) + K_H \nabla_h^2 Fe,$$

$$MIX = \frac{\partial}{\partial z} \left( K_V \frac{\partial Fe}{\partial z} \right),$$
(6)

where *ADV* indicates the dFe flux convergence caused by large-scale flow and lateral mixing that includes the effects of subgrid-scale eddies; *MIX* indicates vertical mixing; *BIO* indicates the source/sink term arising from the biogeochemical processes such as biological uptake, organism degradation, and scavenging; *SED* indicates dFe flux from the sediment source; and *SFX* indicates surface dFe flux supplied from atmospheric dust. The LHS of equation (6) is further divided into two terms as follows:

$$\int_{MLD} \frac{\partial Fe}{\partial t} dz = \frac{\partial}{\partial t} \int_{MLD} Fe dz - \frac{dMLD}{dt} Fe(MLD).$$
(7)

The first term on the RHS of equation (7) is the tendency of dFe concentration within the MLD, and the second term is related to MLD change. As the latter is related to the vertical mixing process, we include it in the *MIX* term in equation (6) in the following budget analysis.

Figure 11 shows the spatial distributions of the annually averaged dFe budget terms as the rate of change of dFe per year. The values of *MIX* and *ADV* are positive over the North Pacific (Figures 11a and 11b), indicating that these terms play a role in the increase of dFe concentration. The *ADV* makes a large contribution to the increase in dFe concentration with a maximum value of 0.9 nM/yr around the Oyashio region (Figure 11b). The *SFX* also contributes positively to the increase in dFe concentration around the Oyashio region (Figure 11d), where dust flux is relatively large (Figure 2a). The value of *BIO* is negative overall and relatively large along the Kuril Islands (Figure 11c). As the spatial pattern of *BIO* is roughly similar to that of the annual average  $\Gamma$  (Figure 7a), negative values of *BIO* are likely explainable by biological uptake rather than scavenging.

Figure 12a shows the seasonal variations of the dFe budget terms in the Oyashio region. In early winter (October–November), the increase in the dFe concentration is explained mostly by *MIX*. However, the contribution of *ADV* is comparable with that of *MIX* in December and it becomes dominant in midwinter (January–March). In the western subarctic region (Figure 12b), *MIX* also makes the largest contribution in early winter (October–November), but *ADV* becomes the largest contributor from mid to late winter (March–April). In both regions, *SFX* makes a small contribution to the increase in dFe concentration from

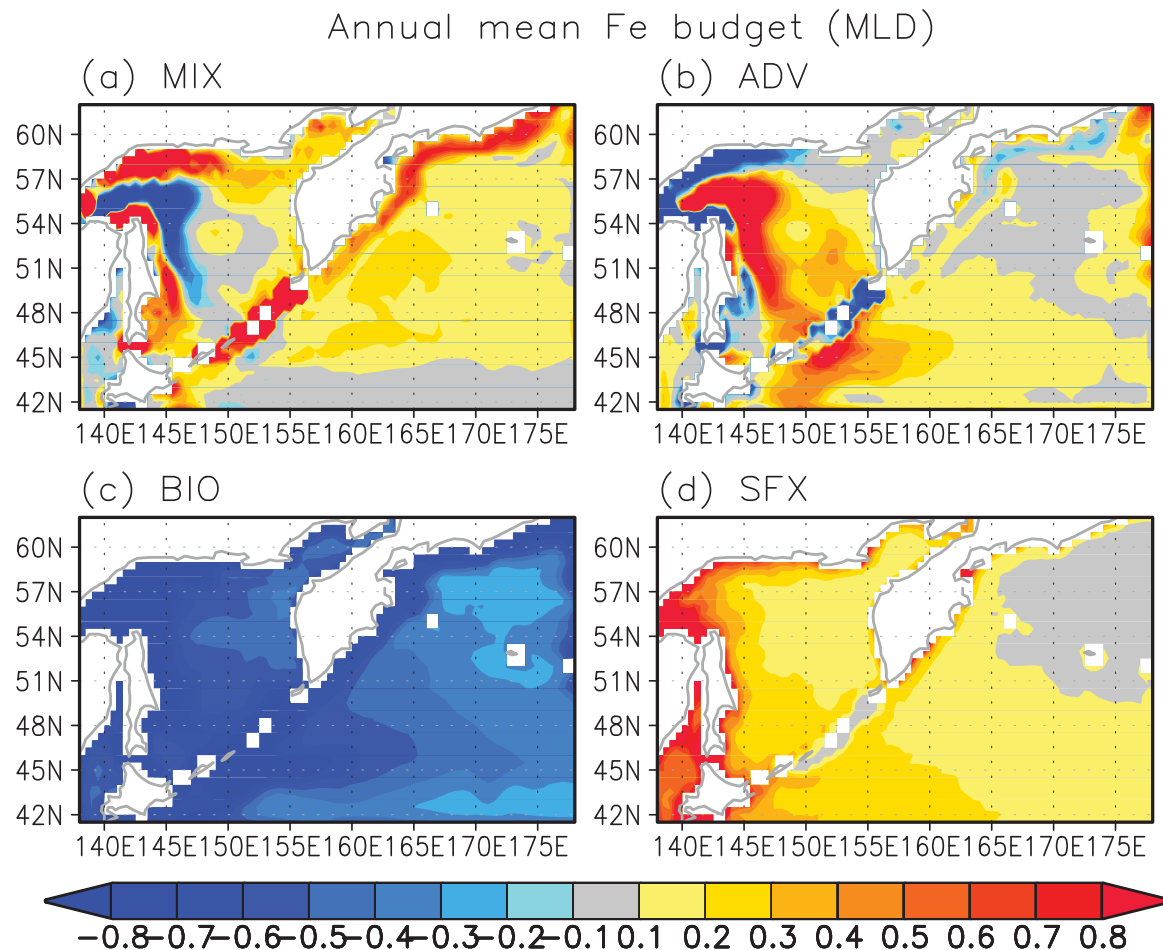


**Figure 11.** Spatial distributions of annual mean (a) *MIX*, (b) *ADV*, (c) *BIO*, and (d) *SFX* terms for the dFe budget ( $\text{nM}/\text{yr}$ ) in the mixed layer.

early to midwinter. For the Oyashio region, the averaged SFX term from early to late winter (November–March) are 0.008 nM/month. This value is 4–5 times less than those for the ADV (0.053 nM/month) and MIX (0.043 nM/month) terms. For the western subarctic region, the SFX term (0.006 nM/month) is still quite smaller than the ADV (0.020 nM/month) and MIX (0.028 nM/month) terms, although the SFX term is the largest contributor from June to August.  $B/I/O$  is always negative with its largest value in spring (May). This seasonality is explained by the seasonal variation of the rate of biological uptake (Figure 8). Thus, the wintertime increase in dFe concentration is controlled by the seasonal cycle of ocean advection and mixing, and the contribution of dust flux is not essential.

Since the dust iron solubility is governed by many factors and processes which have not been clarified yet [Baker and Croot, 2010], it is known to have wide range values from 0.4% [Ooki et al., 2009] to about 6% [Buck et al., 2006]. To check the sensitivity of dust iron solubility to our results, we performed a sensitivity experiment with a dust iron solubility of 2%, which is within the permitting range to form the HNLC in the model [Uchimoto et al., 2014]. The SFX term in this sensitivity experiment is about 2 times larger than the control case, but the fraction of the wintertime dFe concentration is not essentially changed. Thus, the ADV and MIX terms are still dominant on the wintertime increase in the dFe concentration in the target regions. We also performed another sensitivity experiment with a dust iron solubility of 5%, but the seasonal variation in dFe concentration in the Oyashio region is unrealistic (not shown). These sensitivity experiments support that our results on the dFe budget analysis are not sensitive to the dust iron solubility.

To understand the physical mechanism of the *ADV* term, we further divide it into three components: the geostrophic current, ageostrophic current, and lateral mixing process, as follows:

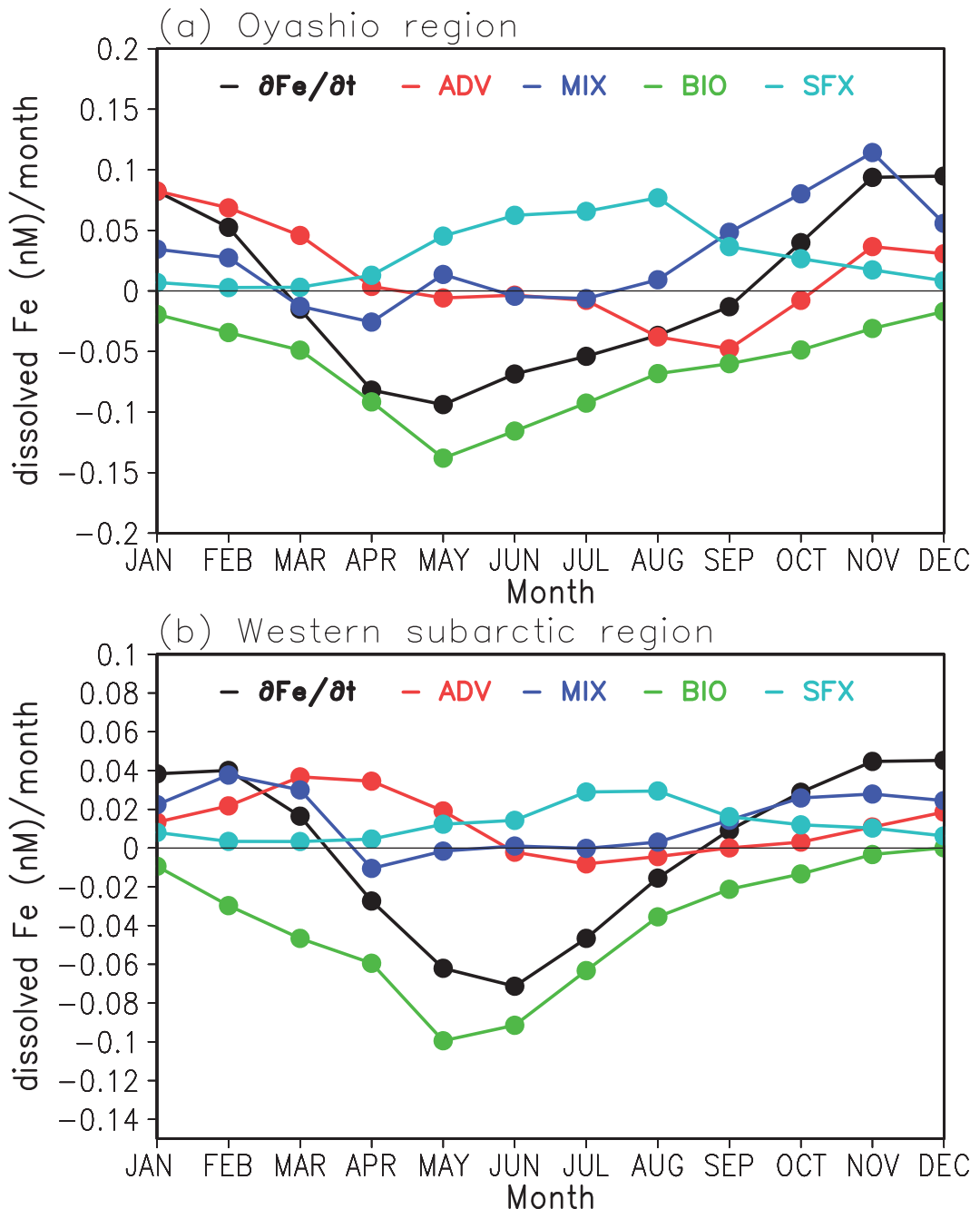


**Figure 12.** Seasonal cycles of each term of the dFe budget (nM/month) averaged in the mixed layer for (a) the Oyashio region and (b) western subarctic region. The tendencies of dFe, ADV, MIX, BIO, and SFX are shown by black, red, blue, green, and cyan lines, respectively.

$$\begin{aligned}
 ADV &= -\nabla \cdot (\vec{v}Fe) + K_H \nabla_h^2 Fe \\
 &= -\nabla \cdot ((\vec{v}_g + \vec{v}_a)Fe) + K_H \nabla_h^2 Fe \\
 &\approx -\underbrace{\vec{v}_g grad_h Fe}_{\text{geo strophic current}} - \underbrace{\vec{v}_a grad_h Fe}_{\text{Ekman transport}} - \underbrace{w_a \frac{\partial Fe}{\partial z}}_{\text{Ekman upwelling}} + \underbrace{K_H \nabla_h^2 Fe}_{\text{lateral mixing}} , \quad (8)
 \end{aligned}$$

where  $v_g$  and  $v_a$  mean the geostrophic and ageostrophic components of the ocean currents, respectively. Here we assume that the horizontal and vertical components of the ageostrophic term (i.e., the second and third terms on the RHS of equation (8)) are related mostly to Ekman transport and Ekman upwelling/

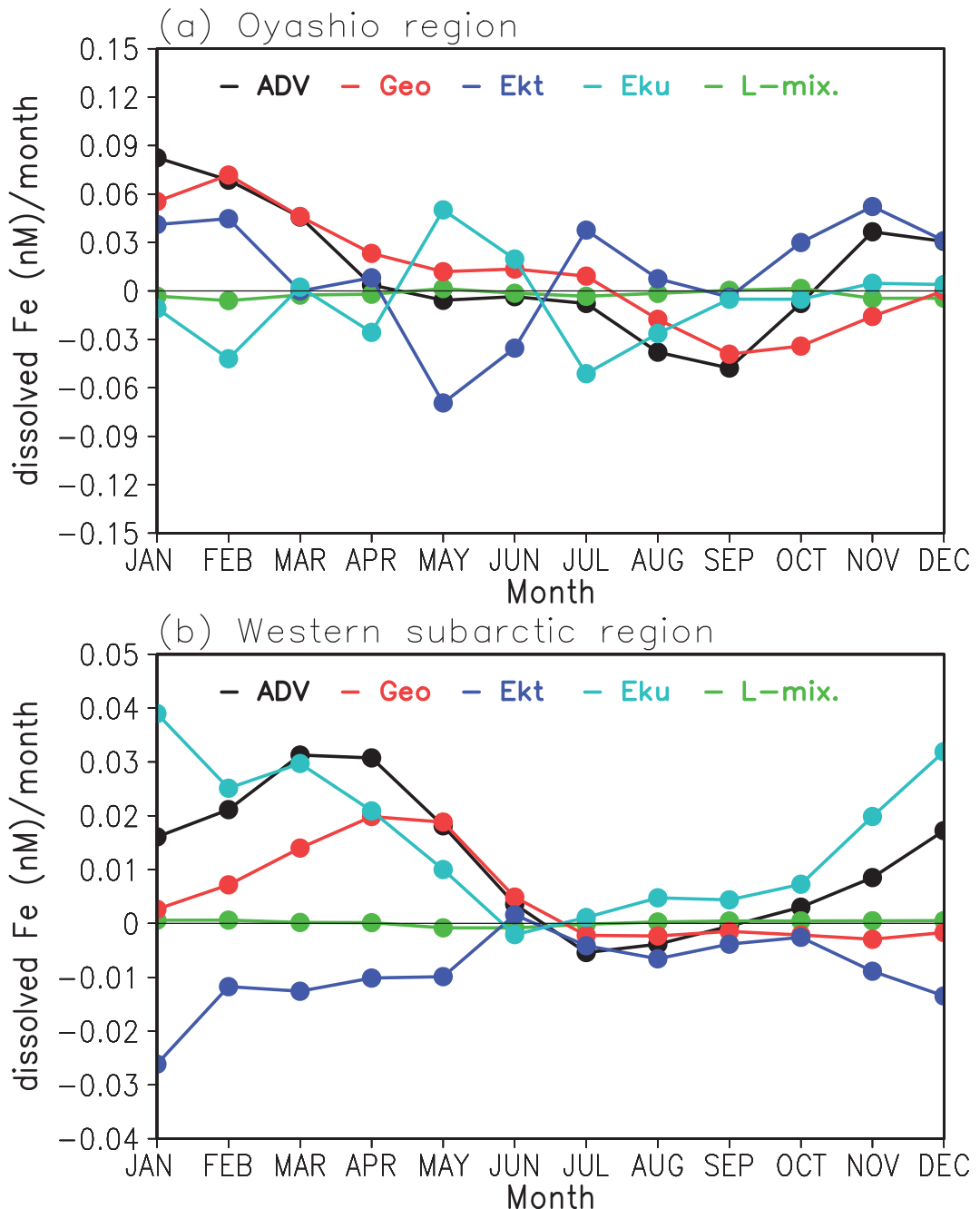


**Figure 13.** Seasonal cycles of dFe convergence (nM/month) of ADV (black) and each component related to the geostrophic current (red), Ekman transport (blue), Ekman upwelling (cyan), and subgrid-scale mixing processes (green) averaged over (a) the Oyashio and (b) western subarctic regions.

downwelling, respectively, because the ageostrophic currents induced by topographic effects are likely to be negligible in the basin area.

Figure 13a shows the seasonal cycles of total ADV averaged in the mixed layer and the related components in the Oyashio region. From November to December, the total ADV is dominated by Ekman transport. Considerable dFe flux convergence because of Ekman transport occurs in the Oyashio region and the southern boundary of the western subarctic gyre ( $42^{\circ}\text{N}$ – $44^{\circ}\text{N}$ ,  $150^{\circ}\text{E}$ – $165^{\circ}\text{E}$ ) (Figure 14a). This dFe flux convergence is related to the southward Ekman transport enhanced by wintertime northerly winds over the WSNP (Figure 14b) and a large meridional gradient of dFe concentration (Figure 14c).

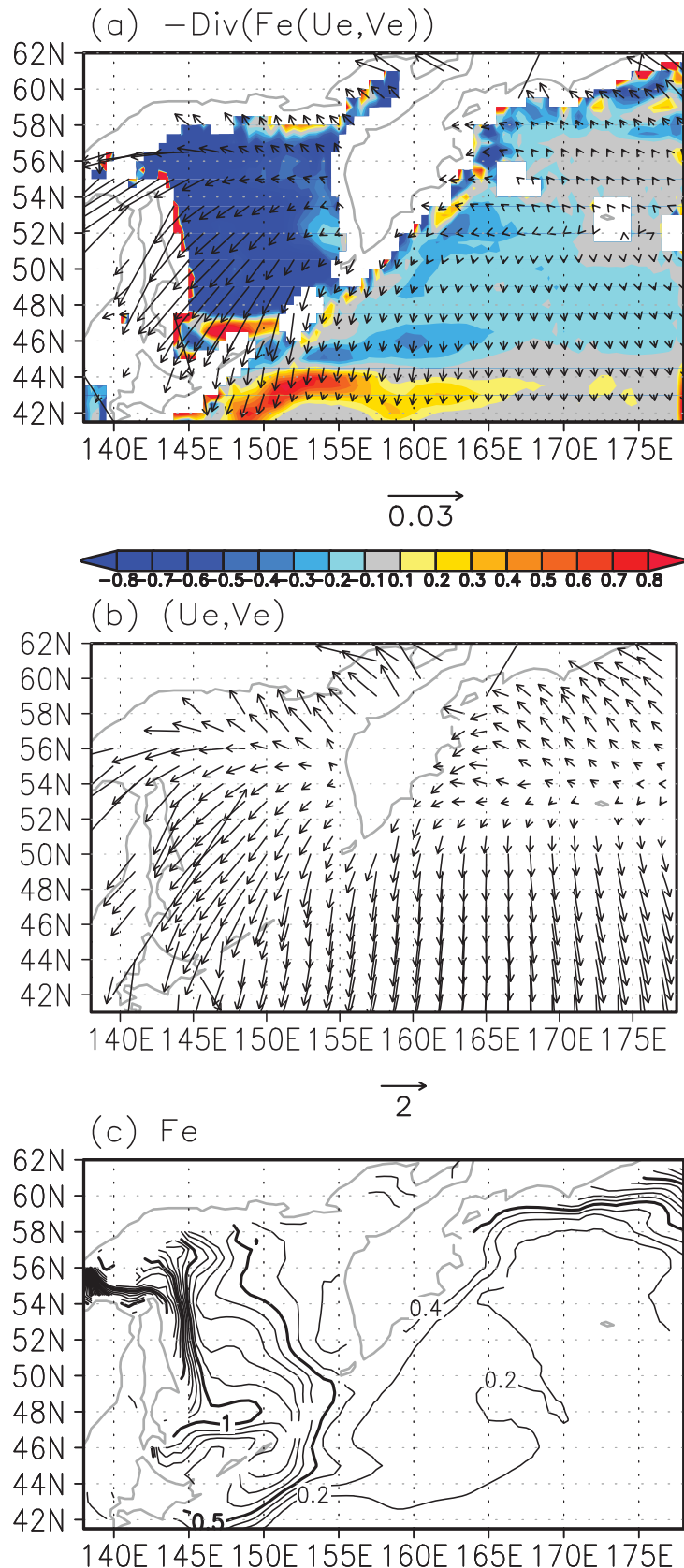


**Figure 14.** Spatial distributions of (a) dFe fluxes related to Ekman transport (vectors:  $\text{nM m/s}$ ) and its convergence ( $\times 10^{-1} \text{nM/month}$ ), (b) Ekman current speed (vectors:  $\text{cm s}^{-1}$ ), and (c) dFe concentration ( $\text{nM}$ ) averaged over the mixed layer from October to the next March.

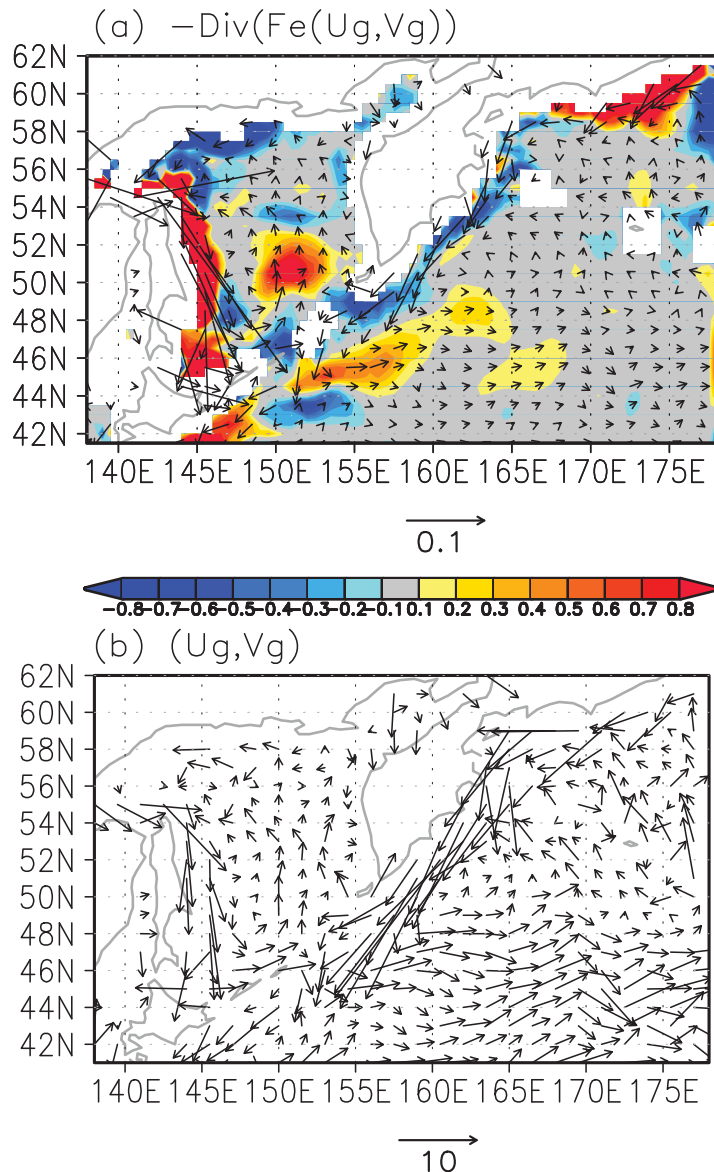


**Figure 15.** Spatial distributions of (a) dFe fluxes related to geostrophic transport (vectors:  $\text{nM m/s}$ ) and its convergence ( $\times 10^{-1} \text{nM/month}$ ), and (b) geostrophic current speed (vectors:  $\text{cm s}^{-1}$ ) averaged over the mixed layer from January to the following March.

in the Oyashio region might be influenced remotely by the advection of dFe-rich water from the Sea of Okhotsk.

In the western subarctic region, the seasonal variation of total ADV is controlled mainly by Ekman upwelling/downwelling (Figure 13b). The spatial distribution of dFe flux convergence related to Ekman upwelling/downwelling from October to the next March reveals the convergence occurs throughout the entire region, except for coastal regions (Figure 16a). In the basin area, the Ekman upwelling is prominent in the mixed layer from October to the next March (Figure 16b). As the averaged vertical gradient of dFe concentration in the MLD is negative (Figure 16c), the wintertime dFe flux convergence is likely to be explained by the combination of the enhanced Ekman upwelling with the climatological vertical dFe gradient.

Careful examination of Figure 13b shows that the seasonal variation of dFe flux convergence due to Ekman upwelling/downwelling is out of phase with that caused by Ekman transport. This implies that part of the upwelled dFe-rich water is transported further southward by Ekman transport, which results in the

In midwinter (January–March), the contribution of the geostrophic current to dFe flux convergence exceeds that of Ekman transport in the Oyashio region (Figure 13a). A remarkable convergence of dFe flux related to the geostrophic component is found in the western part of the Sea of Okhotsk and the Oyashio region (Figure 15a). These regions correspond to the southward western boundary currents in the Sea of Okhotsk and subarctic gyre, which are strengthened by the prevailing wind stress curl in winter [Ohshima et al., 2004; Ioguchi and Kawamura, 2006]. The maximum concentration of dFe is found locally in the northwestern shelf region and Kuril Strait (Figure 14c). The former is likely related to direct advection of dFe-rich water from the source region, while the latter is derived from the intermediate layer through enhanced vertical mixing along the Kuril Strait. Therefore, the dFe flux convergence in the Oyashio region is explained by anomalous ocean currents and the background gradient of dFe concentration. In addition, the outflow of water from the Sea of Okhotsk Sea via the Bussol Strait, which is controlled by a change in the subarctic gyre, is also enhanced in winter [Ohshima et al., 2010]. Thus, the dFe flux convergence

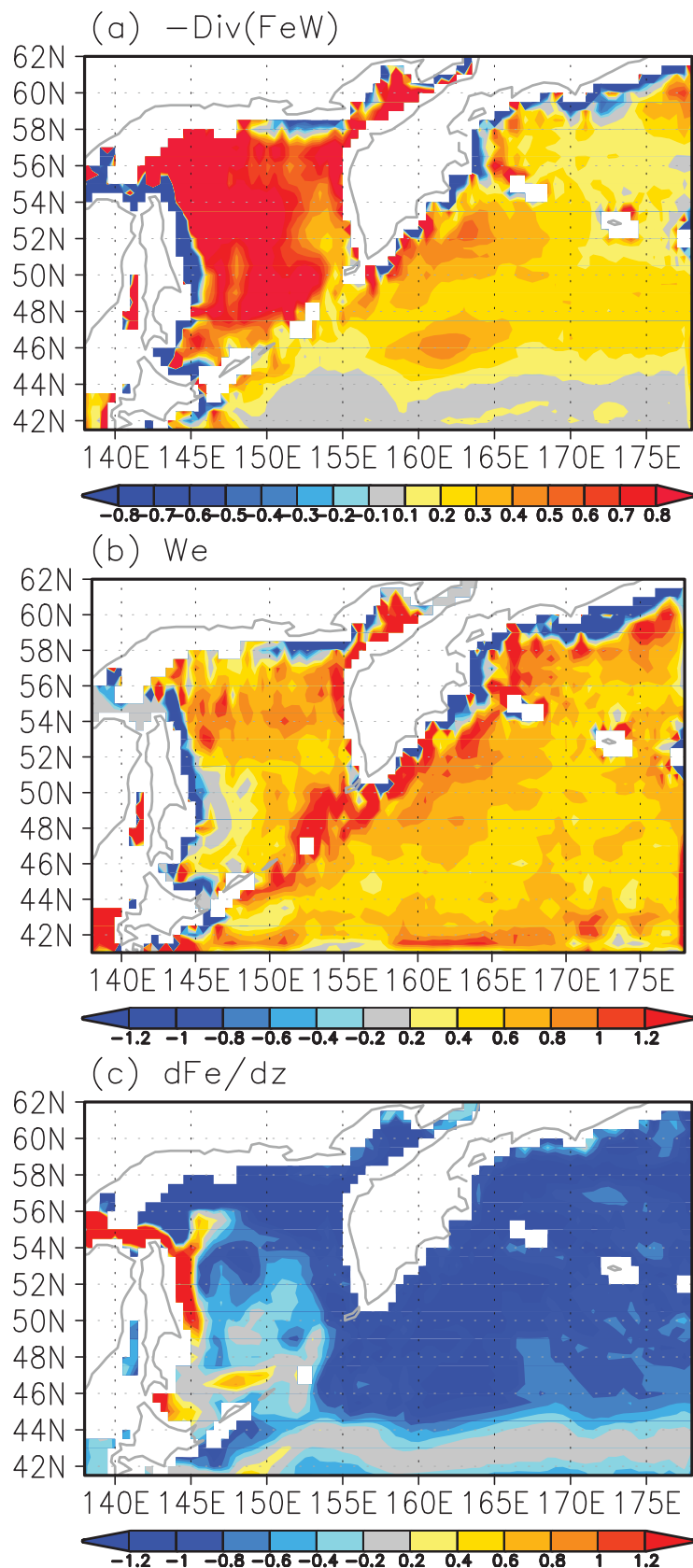


**Figure 16.** Spatial distributions of (a) the convergence of dFe fluxes related to Ekman upwelling/downwelling ( $\times 10^{-1}$  nM/month), (b) vertical component of ocean current ( $\times 10^{-2}$  cm s $^{-1}$ ), and (c) vertical gradient of dFe concentration ( $\times 10^{-3}$  nM m $^{-1}$ ) averaged over the mixed layer from October to the following March.

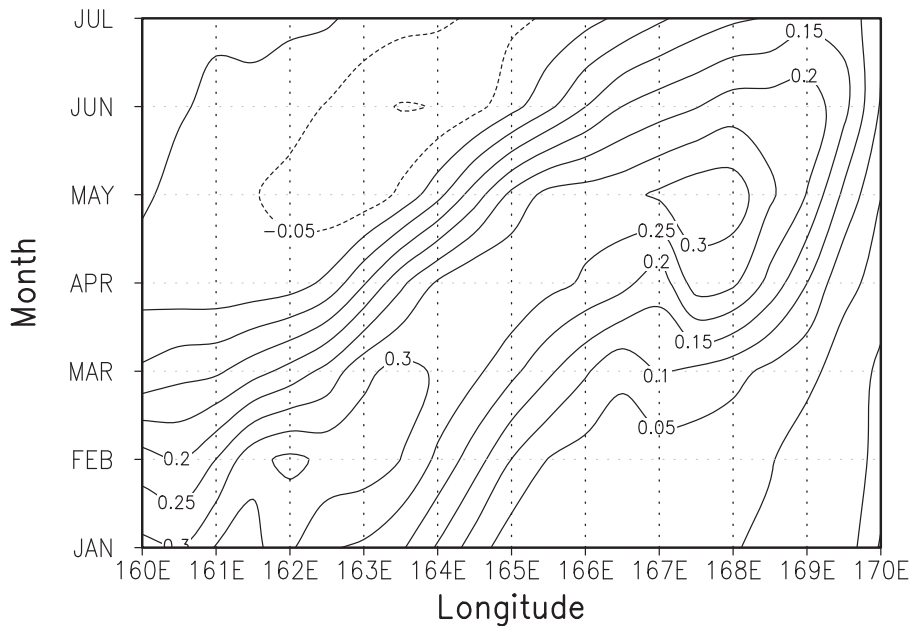


**Figure 17.** Time-longitude cross section of the convergence of dFe fluxes as a result of geostrophic transport (nM/yr) in the mixed layer along 48°N.

generation of a zonal band of dFe flux convergence along the southern part of the subarctic gyre (Figure 14a). In fact, the zonal band of dFe flux convergence (Figure 14a) occurs along the southern edge of the strong dFe flux convergence related to Ekman upwelling/downwelling (Figure 16a). As such an ocean circulation is generated systematically under the influence of midlatitude westerlies, it is suggested that a zonal band of dFe flux convergence generally occurs on the southern boundary of the subarctic gyre.

It is noted that the dFe flux convergence related to the geostrophic current is comparable with that as a result of Ekman upwelling in April–May (Figure 13b). The increase of the contribution of the geostrophic flow occurs about 2 months later than in the Oyashio region (Figure 13a). The spatial distribution of the dFe flux convergence related to the geostrophic current shows a significant anomaly around 48°N, 163°E, extending from the southwest. This is likely caused by the northeastward dFe flux as a result of the subarctic gyre (Figures 15a and 15b). Therefore, the 2 month delay in the increase of dissolved dFe in the western subarctic region is possibly explained by the advection time related to the western subarctic gyre. In fact, the longitude-time section of dFe flux convergence along 48°N shows clear eastward advection from January to April, which is explained by the wintertime mean speed ( $\sim 3.4$  cm/s) of the eastward geostrophic current (Figure 17).

## 5. Origins of Dissolved Fe in the Oyashio Region

The previous section showed that the wintertime increase in dFe concentration in the Oyashio region could be explained mostly by the combination of vertical entrainment and lateral advection. This implies that the contribution of atmospheric dust to the dFe budget is relatively small in comparison with ocean dynamical processes. However, there is a possibility that atmospheric dust injected in upstream regions indirectly affects the dissolved dFe budget in the downstream Oyashio region. To evaluate the contributions of dFe sources, we performed perturbation experiments in which the dFe source was restricted to sediment (SED), atmospheric dust (DUST), and boundary condition (BC) (Table 2). In each experiment, the other sources were fixed to zero values.

Figure 18 shows the seasonal cycle of dFe concentration averaged over the mixed layer in the

**Table 2.** List of Sensitivity Experiments

Experiment	Applied Dissolved Fe Flux
SED	Sediment dissolved Fe flux in the northwestern shelf region
DUST	Surface dust flux over the entire region
BC	Lateral boundary conditions of dissolved Fe

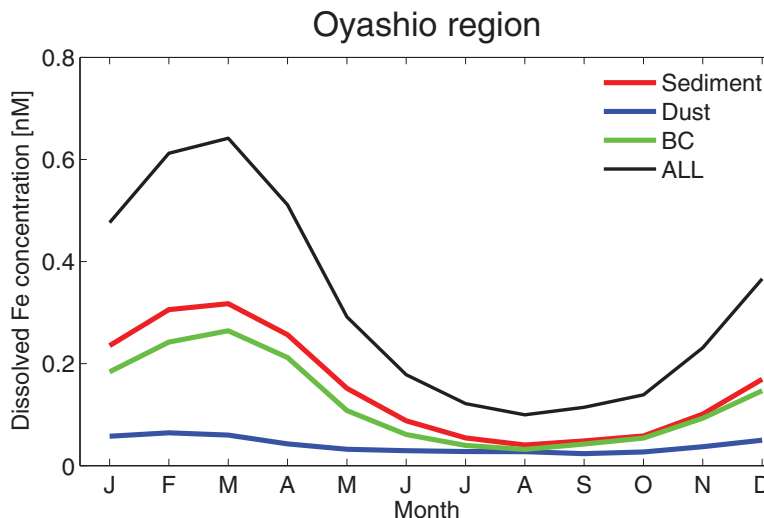


**Figure 18.** Time series of the simulated dFe concentration averaged over the mixed layer in the Oyashio region, calculated from the SED (red), DUST (blue), and BC (green) experiments. The sum of the dFe concentration in the sensitivity experiments is indicated by the black line.

Oyashio region for each sensitivity experiment. The seasonal variation in dFe concentration is explained well by the sum of the SED and BC experiments, and the respective amplitudes of their seasonal variation are similar. In the SED experiment, a high concentration of dFe is found along Sakhalin Island and the Bussol Strait (Figure 19a), suggesting that the southward East Sakhalin Current and vertical mixing in the Kuril Strait are crucial for the transport of dFe to the Oyashio region. Conversely, in the BC experiment, high concentration of dFe is found along the Bering Sea coast and in the Kuril Strait, indicating that dFe originating from the Bering Sea shelf is advected to the Oyashio region together with upward transport by tidal mixing in the Kuril Strait. For the DUST experiment, the dFe concentration shows a weak seasonal cycle with the maximum in February (Figure 18). This result may imply that the dust flux in late summer indirectly influences the wintertime increase of the dFe concentration in the mixed layer through the entrainment and/or lateral advection. However, the seasonal amplitude in the dFe concentration in the DUST experiment is 0.04 nM, which is about 1 order smaller than those in the SED and BC experiments. Here we briefly examined the sensitivity of dust iron solubility on DUST experiment by using a dust iron solubility of 2%. The resultant seasonal amplitude is about 2 times larger than the original DUST experiment (not shown). Thus, these sensitivity experiments support the conclusion of previous studies suggesting that one of the primary sources of dFe in the WSNP is sediment flux on the northwestern shelf of the Sea of Okhotsk [Nishioka *et al.*, 2007], but with a significant contribution from the eastern shelf of the Bering Sea.

## 6. Summary and Discussion

In this study, we quantitatively evaluated the controlling factors of the seasonal variation in dFe concentration in the Oyashio region and the WSNP, using an OGCM coupled with a simple biogeochemical model of PO<sub>4</sub> and dFe cycles [Uchimoto *et al.*, 2014]. In the Oyashio region, the simulated PO<sub>4</sub> and dFe concentrations in the mixed layer showed remarkable seasonal variations with maxima in March, although their amplitudes were half of the observed values. An dFe budget analysis of the mixed layer revealed that the increase in dFe concentration in winter is caused mainly by vertical entrainment as a result of the deepening of the MLD and lateral advection. The lateral advection of dFe in early winter is explained mainly by southwestward Ekman transport, which is driven by the northwesterly wind that prevails over the western subarctic region. In late winter, the dFe flux of lateral advection is also caused by the southwestward geostrophic current.

In the western North Pacific, the increase of dFe concentration in winter is also controlled by entrainment as a result of the deepening of the MLD as in the case of the Oyashio region. However, the advective flux related to Ekman upwelling is comparable with that of the entrainment. The upwelled dFe-rich water is

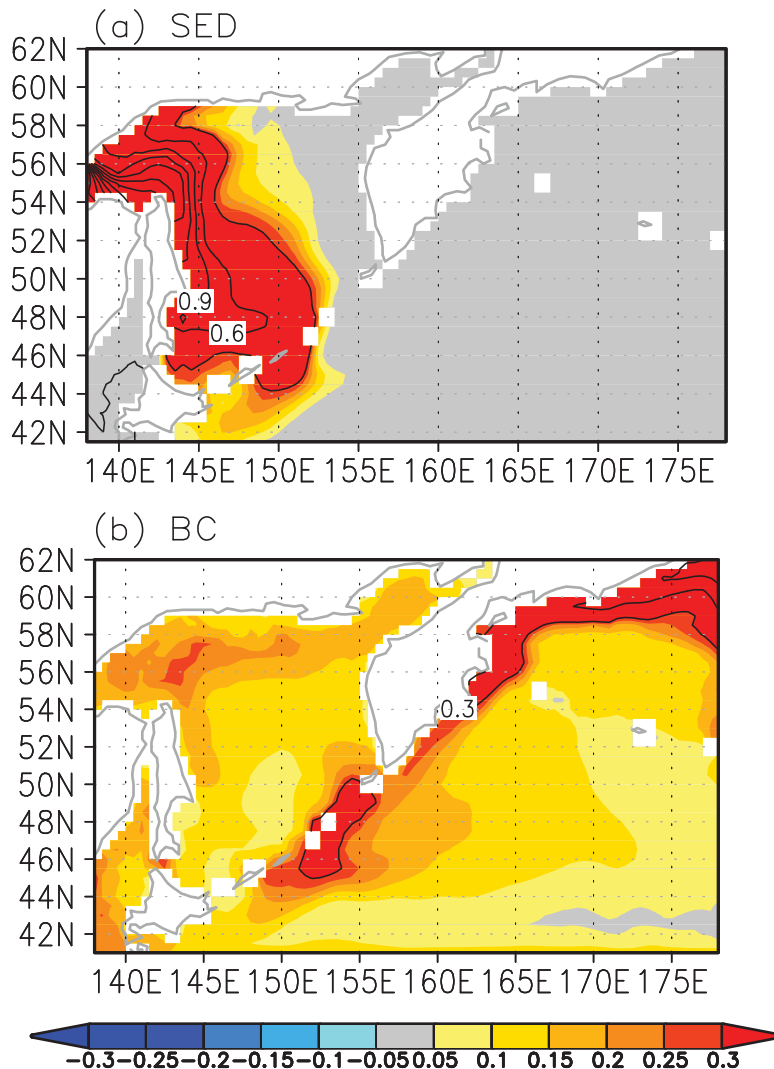
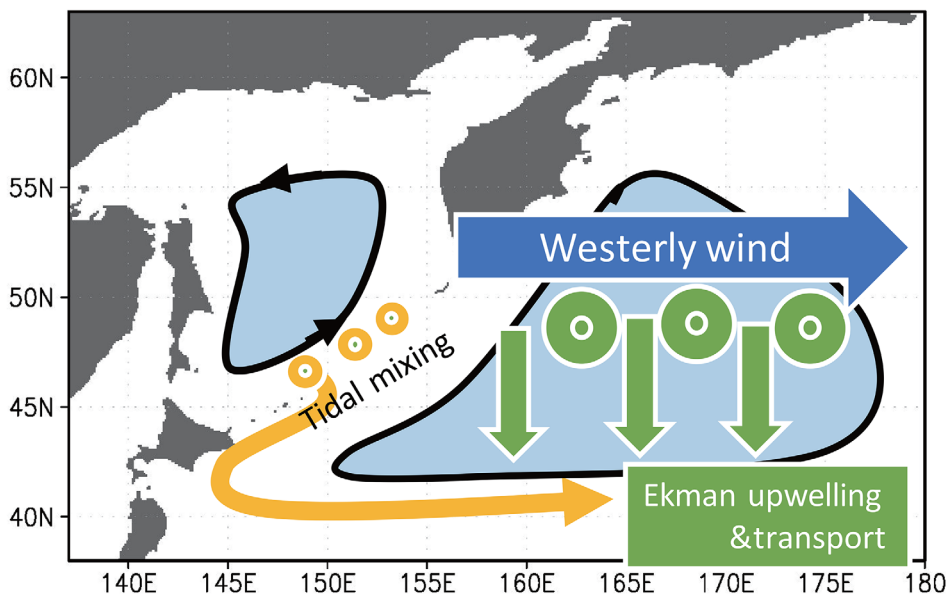


**Figure 19.** Annual mean fields of simulated dFe concentrations (nM, in colors) in the mixed layer, calculated from the (a) SED and (b) BC experiments. Contour intervals are 0.3 nM.

transported further southward by Ekman transport, which is likely to generate a zonal band of dFe flux convergence along the southern boundary of the subarctic gyre. It is noteworthy that the northeastward dFe flux as a result of the subarctic gyre, which is derived from the East Kamchatka Current, is also significant for the increment of dFe concentration in the western subarctic region. Thus, our study supports the suggestion that the combination of Ekman transport and upwelling/downwelling, in addition to the geostrophic current system as well as vertical mixing are important for the seasonal variation of dFe in the WSNP.

The dFe flux and its system of convergence controlled by the wind-driven current in the WSNP are summarized in Figure 20. Under westerly wind conditions, the cyclonic gyre circulation (closed contours) is generated from the surface to the intermediate layer (Figure 20a). In winter, the formation of sea ice leads to subduction over the northwestern shelf region (northwest corner of the basin), and dFe-rich water originating from the source regions, which are the northwestern shelf and Bering Sea shelf (red shaded areas) is transported southward by the western boundary current (yellow arrow) through the intermediate layer (Figure 20b). As tidally induced vertical mixing occurs annually in the Kuril Strait, the dFe-rich water in the intermediate water is fed vertically from the intermediate layer (gray double circles) to the surface layer (yellow double circles), from where it is transported laterally to the downstream region by geostrophic current (yellow line in Figure 20a). The westerly wind also induces both Ekman upwelling (green double circles) and transport (green arrows) over the basin (Figure 20a). As dFe concentration is relatively high in the lower

## (a) Surface layer (Geostrophic+Ekman)



## (b) Intermediate layer (Geostrophic)

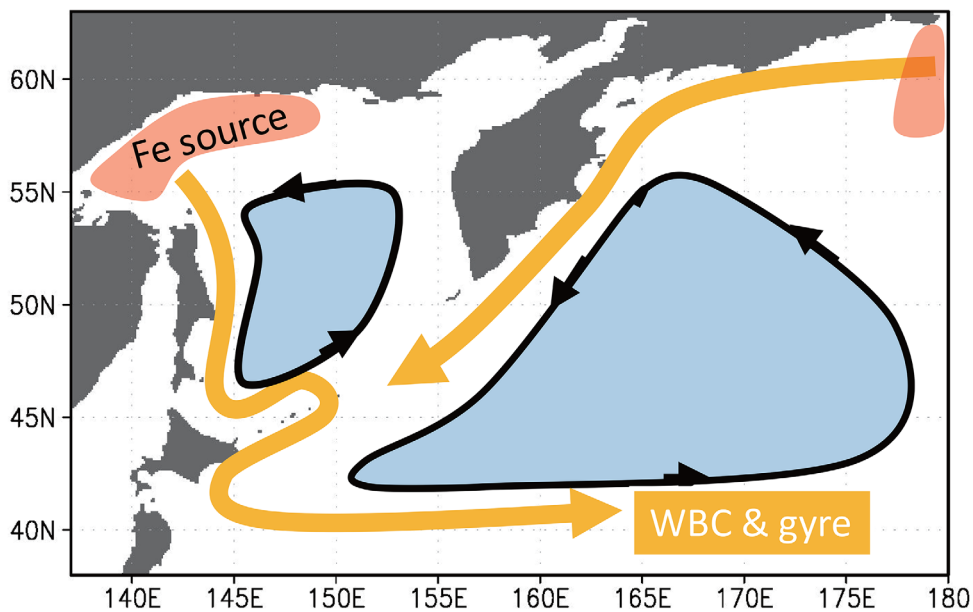


**Figure 20.** Schematics of the surface dFe flux and its convergence system at (a) the surface and (b) intermediate layer in the WSNP, induced by the geostrophic current (yellow arrows) and Ekman transport (green arrows), including Ekman upwelling/downwelling (green double circles), under the condition of midlatitude westerlies (blue arrows) and tidal mixing upwelling (yellow double circles). The closed contours with arrows indicate the cyclonic gyre circulations in the Sea of Okhotsk and WSNP. In Figure 20b, gray double circles indicate the divergence of dFe flux in intermediate layer.

layer, the dFe-rich water upwelled from the intermediate layer (gray double circles) is consequently transported to the southern boundary of the subarctic gyre. As such an ocean circulation is induced systematically over the region affected by the westerly wind, it is suggested that a zonal band of dFe flux convergence generally occurs along the southern boundary of the subarctic gyre.

Atmospheric dust makes a significant contribution to the dFe budget when averaged over the entire year, but the effect is weak from autumn to winter in our model experiments. To check the sensitivity on the

solubility of dust flux, we additionally performed sensitivity experiments on the dust solubility. However, the contributions of lateral advection and vertical mixing are still dominant term on the wintertime increase in the dFe concentration in the Oyashio region, even if the solubility of dust flux increases up to 2%. The sensitivity experiments on the dFe sources (sediment fluxes and atmospheric dust) also support that sediment fluxes in the Sea of Okhotsk and Bering Sea contribute with similar magnitudes to the seasonal variation of surface dFe concentration in the Oyashio region.

On the other hand, there are large uncertainties in the amount of soluble iron in dust, the variability and magnitude of dust flux, and the scavenging parameterization, which are often orders of magnitude, and thus the residence time of dFe concentration has a large uncertainty and shows different values from a year to 100 year timescale among the biogeochemical ocean models [Tagliabue *et al.*, 2016]. Our model experiments control the climatological profiles of dFe by applying the observed dFe concentrations, which probably include both the dust and sediment flux, as the lateral boundary conditions. Therefore, it is difficult to precisely estimate the residence time of atmospheric dust flux and thus precisely identify the origin of the climatological dFe concentration in our model. To clarify the quantitative evaluation of the source for the climatological dFe concentration in the WSNP, further sensitivity experiments on these parameters are needed in basin scale model experiments.

It is noteworthy that dFe-rich water from the Sea of Okhotsk was confined to the Oyashio region and the dFe concentration was quite small in the western subarctic region in the SED experiment. As the dFe concentration is restored to zero at the lateral boundary in the SED experiment, the dFe-rich signal transported from the Sea of Okhotsk is likely damped near the southern boundary. In other words, the SED experiment might underestimate the contribution of sediment dFe flux in the Sea of Okhotsk to the surface dFe concentration in the WSNP. In addition, mesoscale eddies and the coastal Oyashio current, which are important for material transport in the Oyashio region, were not resolved in our model, although subgrid-scale mixing as a result of baroclinic eddies was parameterized. Thus, a numerical study with an eddy-resolving OGCM simulation is needed for further quantitative examination of the physical mechanisms responsible for the transport processes of dFe in the Oyashio and western subarctic regions, which is left for future work.

Recently, it was reported that dFe concentration within the sea ice is 1–2 order higher than the seawater [Tovar-Sánchez *et al.*, 2010; Lannuzel *et al.*, 2010; van der Merwe *et al.*, 2011]. In the Sea of Okhotsk, a large amount of particulate dFe is observed in the sea ice in the southern region [Kanna *et al.*, 2014], implying that sea ice melting leads to dFe supply to the surface layer, which could be advected to the downstream region. Since our biogeochemical model assumes that iron concentration in sea ice is zero, our model may underestimate the lateral advection of dFe from the Okhotsk Sea. In fact, the simulated amplitude of the seasonal variation in the dFe concentration in the Oyashio region is underestimated (Figure 10). To clarify the effect of the dFe flux from sea ice on the seasonal variation in the Oyashio region, an ice-ocean coupled model simulation including the dFe exchange between sea ice and sea as well as the accumulation of dust flux on the snow is desirable.

In this study, we found the wind-driven mechanism controlling the surface dFe concentration in the WSNP, where the wintertime vertical mixing is believed to be an important process on the seasonal variations [Nishioka *et al.*, 2011; Shigemitsu *et al.*, 2012]. The significant contribution of lateral advection on the seasonal variation in the surface dFe concentration is likely attributed to the strong lateral gradient of background dFe concentration. The WSNP is just located near both the Sea of Okhotsk and Gobi Desert, which are major sediment and dust dFe sources, respectively. The tidal mixing in the Kuril Straits locally enhances the increment of surface dFe concentration, which leads to the further strong lateral gradient of dFe. Moreover, the western boundary currents such as the Oyashio current and East Kamchatka Current as well as the cyclonic circulation in the Sea of Okhotsk also have an important role in the transport of Fe-rich water in the northwestern shelf to the North Pacific. Thus, our study suggests that the material circulation and the resultant primary production in WSNP are also susceptible to the wind-driven ocean current change on interannual timescale.

## References

- Baker, A. R., and P. L. Croot (2010), Atmospheric and marine controls on aerosol iron solubility in seawater, *Mar. Chem.*, 120, 4–13.  
Behrenfeld, M. J., and P. G. Falkowski (1997), Photosynthetic rates derived from satellite-based chlorophyll concentration, *Limnol. Oceanogr.*, 42, 1–20, doi:10.4319/lo.1997.42.1.0001.  
Boyd, P. W., et al. (2004), The decline and fate of an iron-induced subarctic phytoplankton bloom, *Nature*, 428, 549–553.

## Acknowledgments

We thank N. Mahowald for providing the dust data set. The WOA data were obtained freely from the United States NODC (<http://data.nodc.noaa.gov/woa/>). The primary production data based on MODIS satellite images were obtained from the Ocean Productivity site of Oregon State University (<http://www.science.oregonstate.edu/ocean.productivity/index.php>). The source code for the ocean model used in this study and input files necessary to reproduce the experiments with Iced-COCO are available from the authors upon request (nakanowatari.takuya@nipr.ac.jp). Numerical calculations were performed using a HITACHI SR16000 at the high-performance computing system of Hokkaido University and an SGI UV1000 at the Pan-Okhotsk Information System of Hokkaido University. We wish to thank two anonymous reviewers for their constructive comments. A number of figures were produced using the GrADS package developed by B. Doty. This work was supported by JSPS KAKENHI (JP22221001, JP20360943, JP16K21586, and JP17H01156), MEXT KAKENHI (JP16H01585), Joint Usage/Research Center for Interdisciplinary Large-scale Information Infrastructures (JHPCN), and the Green Network of Excellence (GREENE) Arctic Climate Change Research Project of the Ministry of Education, Culture, Sports, Science, and Technology in Japan.

- Boyer, T. P., C. Stephens, J. I. Antonov, M. E. Conkright, R. A. Locarnini, T. D. O'Brien, and H. E. Garcia (2002), World ocean atlas 2001: Salinity, in *NOAA Atlas NESDIS 50*, vol. 1, 176 pp., U.S. Gov. Print. Off., Washington, D.C.
- Buck, C. S., W. M. Landing, J. A. Resing, and G. T. Lebon (2006), Aerosol iron and aluminum solubility in the northwest Pacific Ocean: Results from the 2002 IOC cruise, *Geochem. Geophys. Geosyst.*, 7, Q04M07, doi:10.1029/2005GC000977.
- Cullen, J. T., M. Chong, and D. Ianson (2009), British Columbian continental shelf as a source of dissolved iron to the subarctic northeast Pacific Ocean, *Global Biogeochem. Cycles*, 23, GB4012, doi:10.1029/2008GB003326.
- Duce, R. A., and N. W. Tindale (1991), Atmospheric transport of iron and its deposition in the ocean, *Limnol. Oceanogr.*, 36, 1715–1726.
- Garcia, H. E., R. A. Locarnini, T. P. Boyer, J. I. Antonov, M. M. Zweng, O. K. Baranova, and D. R. Johnson (2010), World ocean atlas 2009: Nutrients, in *NOAA Atlas NESDIS 71*, edited by S. Levitus, vol. 4, 398 pp., U.S. Gov. Print. Off., Washington, D.C.
- Hasumi, H. (2006), CCSR ocean component model (COCO) version 4.0, *Tech. Rep. 25*, Cent. for Clim. Syst. Res., Univ. of Tokyo, Chiba, Japan.
- Hunke, E., and J. K. Dukowicz (1997), An elastic-viscous-plastic model for sea ice dynamics, *J. Phys. Oceanogr.*, 27, 1849–1867.
- Isada, T., A. Hattori-Saito, H. Saito, T. Ikeda, and K. Suzuki (2010), Primary productivity and its bio-optical modeling in the Oyashio region, NW Pacific during the spring bloom 2007, *Deep Sea Res., Part II*, 57, 1653–1664.
- Isoguchi, O., and H. Kawamura (2006), Seasonal to interannual variations of the western boundary current of the subarctic North Pacific by a combination of the altimeter and tide gauge sea levels, *J. Geophys. Res.*, 111, C04013, doi:10.1029/2005JC003080.
- Kanna, N., T. Toyota, and J. Nishioka (2014), Iron and macro-nutrient concentrations in sea ice and their impact on the nutritional status of surface waters in the southern Okhotsk Sea, *Prog. Oceanogr.*, 126, 44–57.
- Kawamiya, M., M. J. Kishi, and N. Sugino (2000), An ecosystem model for the North Pacific embedded in a general circulation model Part I: Model description and characteristics of spatial distributions of biological variables, *J. Mar. Syst.*, 25, 129–157.
- Lam, P. J., and J. K. B. Bishop (2008), The continental margin is a key source of iron to the HNLC North Pacific Ocean, *Geophys. Res. Lett.*, 35, L07608, doi:10.1029/2008GL033294.
- Lam, P. J., J. K. B. Bishop, C. C. Henning, M. A. Marcus, G. A. Waychunas, and I. Y. Fung (2006), Wintertime phytoplankton bloom in the subarctic Pacific supported by continental margin iron, *Global Biogeochem. Cycles*, 20, GB1006, doi:10.1029/2005GB002557.
- Lannuzel, D., V. Schoemann, J. de Jong, B. Pasquer, P. van der Merwe, F. Masson, J.-L. Tison, and A. Bowie (2010), Distribution of dissolved iron in Antarctic sea ice: Spatial, seasonal, and inter-annual variability, *J. Geophys. Res.*, 115, G03022, doi:10.1029/2009JG001031.
- Mahowald, N., A. Baker, G. Bergametti, N. Brooks, R. Duce, T. Jickells, N. Kubilay, J. Prospero, and I. Tegen (2005), Atmospheric global dust cycle and iron inputs to the ocean, *Global Biogeochem. Cycles*, 19, GB4025, doi:10.1029/2004GB002402.
- Martin, J. H., G. A. Knauer, D. M. Karl, and W. W. Broenkow (1987), VERTEX: Carbon cycling in the northeast Pacific, *Deep Sea Res., Part I*, 34, 267–285, doi:10.1016/0198-0149(87)90086-0.
- Martin, J. H., R. M. Gordon, S. Fitzwater, and W. W. Broenkow (1989), VERTEX: Phytoplankton/iron studies in the Gulf of Alaska, *Deep Sea Res., Part I*, 36, 649–680, doi:10.1016/0198-0149(89)90144-1.
- Measures, C. I., M. T. Brown, and S. Vink (2005), Dust deposition to the surface waters of the western and central North Pacific inferred from surface water dissolved aluminium concentrations, *Geochem. Geophys. Geosyst.*, 6, Q09M03, doi:10.1029/2005GC000922.
- Misumi, K., et al. (2011), Mechanisms controlling dissolved iron distribution in the North Pacific: A model study, *J. Geophys. Res.*, 116, G03005, doi:10.1029/2010JC001541.
- Moore, J. K., S. C. Doney, and K. Lindsay (2004), Upper ocean ecosystem dynamics and iron cycling in a global three-dimensional model, *Global Biogeochem. Cycles*, 18, GB4028, doi:10.1029/2004GB002220.
- Nakamura, T., and T. Awaji (2004), Tidally induced diapycnal mixing in the Kuril Straits and its role in water transformation and transport: A three-dimensional non-hydrostatic model experiment, *J. Geophys. Res.*, 109, C09S07, doi:10.1029/2003JC001850.
- Nakanowatari, T., T. Nakamura, K. Uchimoto, H. Uehara, H. Mitsudera, K. I. Ohshima, H. Hasumi, and M. Wakatsuchi (2015), Causes of the multidecadal-scale warming of the intermediate water in the Okhotsk Sea and western subarctic North Pacific, *J. Clim.*, 28, 714–736.
- Nishioka, J., et al. (2007), Iron supply to the western subarctic Pacific: Importance of iron export from the Sea of Okhotsk, *J. Geophys. Res.*, 112, C10012, doi:10.1029/2006JC004055.
- Nishioka, J., T. Ono, H. Saito, K. Sakaoka, and T. Yoshimura (2011), Oceanic iron supply mechanisms which support the spring diatom bloom in the Oyashio region, western subarctic Pacific, *J. Geophys. Res.*, 116, C02021, doi:10.1029/2010JC006321.
- Nishioka, J., et al. (2013), Intensive mixing along an island chain controls oceanic biogeochemical cycles, *Global Biogeochem. Cycles*, 27, 920–929, doi:10.1002/gbc.20088.
- Nishioka, J., T. Nakatsuka, K. Ono, Y. N. Volkov, A. Scherbini, and T. Shiraiwa (2014), Quantitative evaluation of iron transport processes in the Sea of Okhotsk, *Prog. Oceanogr.*, 126, 180–193.
- Ohshima, K. I., D. Simizu, M. Itoh, G. Mizuta, Y. Fukamachi, S. C. Risner, and M. Wakatsuchi (2004), Sverdrup balance and the cyclonic gyre in the Sea of Okhotsk, *J. Phys. Oceanogr.*, 34, 513–525.
- Ohshima, K. I., T. Nakanowatari, S. C. Risner, and M. Wakatsuchi (2010), Seasonal variation in the in- and outflow of the Okhotsk Sea with the North Pacific, *Deep Sea Res., Part II*, 57, 1247–1256.
- Ooki, A., J. Nishioka, T. Ono, and S. Noriki (2009), Size dependence of iron solubility of Asian mineral dust particles, *J. Geophys. Res.*, 114, D03202, doi:10.1029/2008JD010804.
- Parekh, P., M. J. Follows, and E. A. Boyle (2005), Decoupling of iron and phosphate in the global ocean, *Global Biogeochem. Cycles*, 19, GB2020, doi:10.1029/2004GB002280.
- Parekh, P., F. Joos, and A. Müller (2008), A modeling assessment of the interplay between aeolian iron fluxes and iron-binding ligands in controlling carbon dioxide fluctuations during Antarctic warm events, *Paleoceanography*, 23, PA4202, doi:10.1029/2007PA001531.
- Perovich, D. K. (1998), The optical properties of sea ice, in *Physics of Ice-Covered Seas*, vol. 1, edited by M. Leppäranta, pp. 195–230, Helsinki Univ. Press, Helsinki.
- Röske, F. (2001), An atlas of surface fluxes based on the ECMWF re-analysis—A climatological dataset to force global ocean general circulation models, Rep. 323, 31 pp., Max-Planck-Inst. für Meteorol., Hamburg, Germany.
- Saito, H., A. Tsuda, and H. Kasai (2002), Nutrient and plankton dynamics in the Oyashio region of the western subarctic Pacific, *Deep Sea Res., Part II*, 49, 5463–5486.
- Sakurai, Y. (2007), An overview of Oyashio ecosystem, *Deep Sea Res., Part II*, 54, 2526–2542.
- Sarmiento, J. L., R. D. Slater, M. J. R. Fasham, H. W. Ducklow, J. R. Toggweiler, and G. T. Evans (1993), A seasonal three-dimensional ecosystem model of nitrogen cycling in the North Atlantic euphotic zone, *Global Biogeochem. Cycles*, 7, 417–450.
- Semtner, A. J., Jr. (1976), A model for the thermodynamic growth of sea ice in numerical investigations of climate, *J. Phys. Oceanogr.*, 6, 379–389.

- Shigemitsu, M., T. Okunishi, J. Nishioka, H. Sumata, T. Hashioka, M. N. Aita, S. L. Smith, N. Yoshie, N. Okada, and Y. Yamanaka (2012), Development of a one-dimensional ecosystem model including the iron cycle applied to the Oyashio region, western subarctic Pacific, *J. Geophys. Res.*, 117, C06021, doi:10.1029/2011JC007689.
- Siegel, D. A., S. C. Doney, and J. A. Yoder (2002), The North Atlantic spring phytoplankton bloom and Sverdrup's critical depth hypothesis, *Science*, 296, 730–733.
- Stephens, C., J. I. Antonov, T. P. Boyer, M. E. Conkright, R. A. Locarnini, T. D. O'Brien, and H. E. Garcia (2002), World ocean atlas 2001: Temperature, in *NOAA Atlas NESDIS 49*, vol. 1, 176 pp., U.S. Gov. Print. Off., Washington, D. C.
- Tagliabue, A., O. Aumont, R. DeAth, J. P. Dunne, S. Dutkiewicz, E. Galbraith, K. Misumi, J. K. Moore, A. Ridgwell, E. Sherman, et al. (2016), How well do global ocean biogeochemistry models simulate dissolved iron distributions?, *Global Biogeochem. Cycles*, 30, 149–174, doi:10.1002/2015GB005289.
- Takahashi, T., et al. (2002), Global sea-air CO<sub>2</sub> flux based on climatological surface ocean pCO<sub>2</sub>, and seasonal biological and temperature effects, *Deep Sea Res., Part II*, 49, 1601–1622.
- Takata, H., K. Kuma, S. Iwade, Y. Isoda, H. Kuroda, and T. Senju (2005), Comparative vertical distributions of iron in the Japan Sea, the Bering Sea, and the western North Pacific Ocean, *J. Geophys. Res.*, 110, C07004, doi:10.1029/2004JC002783.
- Takata, H., K. Kuma, Y. Isoda, S. Otosaka, T. Senju, and M. Minagawa (2008), Iron in the Japan Sea and its implications for the physical processes in deep water, *Geophys. Res. Lett.*, 35, L02606, doi:10.1029/2007GL031794.
- Tanaka, Y., T. Hibiya, Y. Niwa, and N. Iwamae (2010), Numerical study of K<sub>i</sub> internal tides in the Kuril Straits, *J. Geophys. Res.*, 115, C09016, doi:10.1029/2009JC005903.
- Tovar-Sánchez, A., C. M. Duarte, J. C. Alonso, S. Lacorte, R. Tauler, and C. Galbán-Malagón (2010), Impacts of metals and nutrients released from melting multiyear Arctic sea ice, *J. Geophys. Res.*, 115, C07003, doi:10.1029/2009JC005685.
- Tsuda, A., et al. (2003), A mesoscale iron enrichment in the western subarctic Pacific induces large centric diatom bloom, *Science*, 300, 958–961.
- Uchimoto, K., T. Nakamura, J. Nishioka, H. Mitsudera, M. Yamamoto-Kawai, K. Misumi, and D. Tsumune (2011), Simulations of chlorofluorocarbons in and around the Sea of Okhotsk: Effects of tidal mixing and brine rejection on the ventilation, *J. Geophys. Res.*, 116, C02034, doi:10.1029/2010JC006487.
- Uchimoto, K., T. Nakamura, J. Nishioka, H. Mitsudera, K. Misumi, D. Tsumune, and M. Wakatsuchi (2014), Simulation of high concentration of iron in dense shelf water in the Okhotsk Sea, *Prog. Oceanogr.*, 126, 194–210.
- van der Merwe, P., D. Lannuzel, A. R. Bowie, C. A. Mancuso Nichols, and K. M. Meiners (2011), Iron fractionation in pack and fast ice in East Antarctica: Temporal decoupling between the release of dissolved and particulate iron during spring melt, *Deep Sea Res., Part II*, 58, 1222–1236.